Structure analyses of cellobiose and cellulose using X-ray diffraction and solid-state NMR spectroscopy on oriented samples

Guangjie SONG

2015

Contents

Chapter 1

Background of the study

1.1 Importance of structure analyses of cellulose

Cellulose is one of the most abundant biomaterials on the earth and has drawn increasing attention as a renewable, biocompatible and degradable material.[1, 2] Currently, it is highly demanded to expand the utilization of cellulose in the wider areas in high end-use. The structural analysis of cellulose is a key to this goal because the structures and properties are closely related; the understanding of structures is essential to improve the properties in final products.[1-3]

Cellulose is synthesized by enzymatic polymerization, crystallized, organized to nano-crystals (CNC), and self-assembled in microfibers. It is further organized into cell walls, fibers, etc. Biosyntheses at terminal complexes [2] are diverse depending on biological sources, resulting in diversities in subsequent morphologies of cellulose.[2] Two crystal forms, I_α and I_β, determined by diffraction [4] and spectroscopic methods [5] are known. Size and shape of CNCs depend on sources. Organizations and orientations of CNCs in microfibers and fibers are diverse. All these hierarchical diversities in structure make it difficult to characterize the physical, chemical, and biological properties of cellulose. It is evident that structures should be elucidated at every level of hierarchies, however, structures exhibited are so complicated.

In this thesis, attempts are made to develop methods to elucidating some aspects of cellulose structures. Techniques of magnetic orientation of crystals and fibers are used to prepare oriented samples that are analyzed by X-ray diffractions and solid-state NMR spectroscopy. By orientation, it becomes possible for the first time to obtain more

information on structures. In this thesis, magnetically oriented cellobiose (a smallest repeating unit of cellulose) crystals and cellulose whiskers are studied. X-ray diffraction and solid-state NMR techniques are used to elucidate the solid state structure of these materials. These two techniques are powerful to analyze solid state structures and mutually complementary. In chapter 2, the diamagnetic anisotropy of cellobiose is determined, which provides the experimental conditions needed to prepare the oriented samples. In chapter 3, the chemical shift tensors of C1 and C1' carbons of cellobiose crystals are determined using magnetically oriented samples. In chapter 4, magnetically oriented cellulose whiskers are analyzed by X-ray diffraction and the correlation lengths of CNC orientations are determined.

1.2 Methods used

1.2.1 X-ray diffraction

X-ray is scattered by electrons in the crystals, and the periodic electron density in the crystal results in the diffraction. Therefore, the X-ray can be scattered by heavy atoms (having more electrons) more strongly than light atoms such as hydrogen atoms.[6]

There are three major ways of performing X-ray diffraction measurements. Single crystal X-ray diffraction method is most powerful and accurate in atomic level structure determination of crystals. However, it is sometimes difficult to grow a single crystal large enough to apply this method; crystals about 100 μm are needed though much smaller ones suffice if synchrotron sources are used. Fiber diffraction method is applied to fibrous materials including synthetic polymeric fiebers such as poly(ethylene terephthalate), nylon, etc. and bio-fibers such as cellulose, silk, collagen, etc.

Micro/nano crystals are uniaxially distributed in fibers and the single crystal approach is unavailable. However, the three-dimensional information of the crystal structures is partially retained in fiber diffractions. Powder diffraction method is used when crystals are available as a powder. As described in this thesis, there is an alternative way. A powder sample can be magnetically aligned three-dimensionally in a polymeric matrix material, which we call MOMA (Magnetically Oriented Microcrystal Array). A MOMA can diffract in a similar way to a real single crystal.

1.2.2 Solid-state NMR

Unlike diffraction methods, solid-state NMR spectroscopy is suited for looking at local electric environments around specific resonating nuclei. These environments reflect on host-guest structures, absorptions, and hydrogen bondings, etc.[7] The local structures in crystals are also of great interest because they are strongly related to the inter- and intra-interactions of molecules in crystalline states. The local electric distributions are reflected on several NMR parameters including chemical shift tensors.

Chemical shift is one of most frequently used NMR parameters. Because of Larmor precession induced by an applied magnetic field, the magnetic field applied on a nucleus is shielded. As a result, the resonance frequency is shifted from where it should be without Larmor precession. This shift is referred to as chemical shift. If the shielding is anisotropic, then, the chemical shift cannot be a scalar, but it should be a tensor. This tensor is referred to chemical shift tensor.

The chemical shift tensor is described by three principal values σ_1, σ_2, and σ_3, and three principal axes. With the conventional one-dimensional NMR at magic angle spinning, only the average of the principal values is observed. Without magic angle

spinning we obtain powder patterns, from which three principal values can be determined in principal. In order to determine the principal axes, we need to perform measurements on a single crystal.

Similar to the X-ray diffraction method, preparation of a large single crystal is a bottleneck for single crystal NMR measurements. In many circumstances, large single crystals (millimeter sizes) are difficult to prepare.

1.2.3 Magnetic orientation

As we discussed above, X-ray diffraction and NMR spectroscopy on oriented sample can give rise to more enhanced structural information. The orientation can be achieved using external fields like magnetic fields, mechanical field, and electric field. In this thesis, we choose magnetic fields to align microcrystals.

1.2.3.1 Magnetic susceptibility of diamagnetic crystals [8]

Magnetic susceptibility tensor χ of crystals is expressed by three principal values χ_1, χ_2, and χ_3 that are all negative because diamagnetic crystals are concerned. We define $\chi_3 \le \chi_2 \le \chi_1 < 0$. Crystals are classified into three types: biaxial, uniaxial, and isotropic. (i) Biaxial crystals include the triclinic, monoclinic, and orthorhombic systems. Three principal values are different from one another, i.e., $\chi_3 < \chi_2 < \chi_1$. In orthorhombic crystals, three magnetic axes correspond to three crystallographic *a*, *b*, and *c* axes. In monoclinic crystals, two fold rotation or inversion axis corresponds to one of χ values. In triclinic crystals, there are no fixed relations between susceptibility axes and crystallographic axes. (ii) Uniaxial crystals include the trigonal, hexagonal, and tetragonal systems. Two of χ values are equal, i.e., $\chi_3 = \chi_2 < \chi_1$ or $\chi_3 < \chi_2 = \chi_1$. 3-, 6-, and 4-fold crystallographic axes of trigonal, hexagonal, and

tetragonal crystals, respectively, correspond to one of susceptibility axes. (iii) Isotropic crystals include cubic system, for which $\chi_3 = \chi_2 = \chi_1$.

1.2.3.2 Magnetic energy

The anisotropic magnetic energy of a piece of crystal of volume V subjected to an external magnetic field $\mathbf{B} = {}^{t}(B_1, B_2, B_3)$ (t indicating transpose) is expressed by

$$E = -\frac{V}{2\mu_0} {}^{t}\mathbf{B}\boldsymbol{\chi}\mathbf{B}, \qquad (1)$$

where the magnetic susceptibility tensor $\boldsymbol{\chi}$ and the magnetic field $\mathbf{B}$ are expressed relative to the laboratory $x_1x_2x_3$ frame. The tensor $\boldsymbol{\chi}$ is transformed into $\boldsymbol{\chi}'$ with respect to the particle frame. $\boldsymbol{\chi}'$ is diagonalized and diagonal components are χ_1, χ_2, and χ_3. The tensors $\boldsymbol{\chi}$ and $\boldsymbol{\chi}'$ are related through the transformation matrix $\mathbf{A}$ as follows:

$$\boldsymbol{\chi} = {}^{t}\mathbf{A}\boldsymbol{\chi}'\mathbf{A}, \qquad (2)$$

where the matrix $\mathbf{A}$ is expressed using Eulerian angles. [9] Then, eq.(1) is rewritten as

$$E = -\frac{V}{2\mu_0} {}^{t}\mathbf{B}\, {}^{t}\mathbf{A}\boldsymbol{\chi}'\mathbf{A}\mathbf{B}. \qquad (3)$$

1.2.3.3 Magnetic orientation

Magnetic orientation of any crystal systems under any applied magnetic fields are

derived from eq.(3). For example, in the case of uniaxial crystals ($\chi_3 = \chi_2 < \chi_1$) subjected to a static magnetic field $\mathbf{B} = {}^{t}(0,0,B)$, we obtain

$$E = -\frac{VB^2}{2\mu_0}(\chi_1 - \chi_3)\cos^2\alpha, \qquad (4)$$

where α is the angle between the magnetic field and χ_1 axis. *E* has a minimum at α = 0; that is, $\chi_1 || \mathbf{B}$, indicating that the χ_1 axis aligns parallel to the applied magnetic field [**Fig. 1a**].

In the case of uniaxial crystals ($\chi_3 < \chi_2 = \chi_1$) subjected to a rotating magnetic field $\mathbf{B} = {}^{t}(B\cos\omega t, B\sin\omega t, 0)$ (*t* is time) at rotation frequency of ω, we obtain

$$\langle E \rangle = -\frac{B^2 V}{4\mu_0}(\chi_1 - \chi_3)\cos^2\beta, \qquad (5)$$

where eq.(3) is time-averaged over one revolution and β is the angle between the rotation axis and the χ_3 axis. <*E*> has a minimum at $\beta = 0$; that is, χ_3 axis aligns parallel to the rotation axis [**Fig. 1b**].

In the case of biaxial crystals $\chi_3 < \chi_2 < \chi_1$ subjected to an amplitude-modulated rotating magnetic field, $\mathbf{B} = {}^{t}(B_1\cos\omega t, B_2\sin\omega t, 0)$, where $B_1 > B_2$, we can achieve three-dimensional alignment in which $\chi_1 || x_1$, $\chi_2 || x_2$, $\chi_3 || x_3$ [**Fig. 1c**].

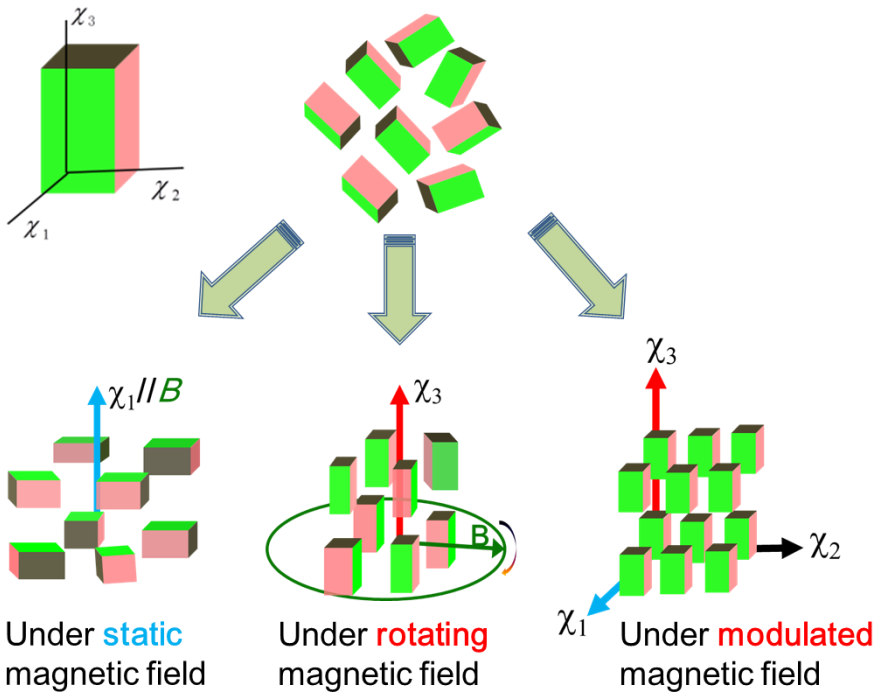

Fig. 1 Different orientation states under three types of magnetic fields

1.3 Objective of my PhD research

The objective of my PhD research is to analyze the structures of cellobiose and cellulose with X-ray diffraction and solid state NMR spectroscopy by using oriented microcrystalline samples.

1.4 The outline of my thesis

Chapter 1 Background of the study

Chapter 2 Determination of anisotropic diamagnetic susceptibility of cellobiose crystals

by performing X-ray diffraction measurement

In this chapter, we present a facile method for determining the anisotropic diamagnetic susceptibility of biaxial crystals by performing X-ray diffraction measurements. The proposed method is based on the fact that the amplitude of fluctuations in a crystallographic axis under a magnetic field depends on the direction of the field with respect to the susceptibility axes. By calculating the magnetic energies of a crystal under static and rotating magnetic fields, we determined the relationship of the half-width of the diffraction spots corresponding to the (*hkl*) planes with the anisotropic magnetic susceptibilities $\chi_1 - \chi_2$ and $\chi_2 - \chi_3$ for the static field and $\chi_1 - \chi_2$ and $\chi_1 - \chi_3$ for the rotating field, where $\chi_1 > \chi_2 > \chi_3$. We have shown that the absolute values of the anisotropic diamagnetic susceptibilities can be determined if the size of the microcrystals is known, whereas only the ratio $(\chi_2 - \chi_3)/(\chi_1 - \chi_2)$ or $(\chi_1 - \chi_3)/(\chi_1 - \chi_2)$ can be determined if the microcrystal size is unknown.

The developed method was applied to cellobiose microcrystal. The ratio of diamagnetic anisotropy of cellobiose (monoclinic, space group $P2_1$) was determined using two X-ray fiber diffraction patterns that were obtained from its microcrystalline powder oriented in static and rotating magnetic fields. We first determined the directions of the magnetic axes with respect to the crystallographic axes to obtain that χ_3 is parallel to the b^* axis and the χ_1 axis makes angles of 67.9° and 22.8° with respect to the a^* and c^* axes, respectively. Following the analysis method proposed recently, azimuthal half widths of the X-ray diffraction spots for (*hkl*) planes of the oriented samples were plotted as a function of $\sin^2\Phi$, where Φ is an angle that characterizes the direction of the reciprocal vector of the (*hkl*) plane in the $\chi_1\chi_2\chi_3$ coordinates, with χ_1, χ_2, and χ_3 being the principal axes of the magnetic

susceptibility tensor. The half width linearly depended on $\sin^2 \Phi$ as predicted by the proposed method. From the values of the slope and intercept of the plot, the ratio of the diamagnetic anisotropy, $r_\chi = (\chi_2 - \chi_3)/(\chi_1 - \chi_2)$ was determined, where $\chi_1 > \chi_2 > \chi_3$. We estimated that r_χ = 1.4~1.7.

Chapter 3 Determination of the chemical shift tensors of cellobiose by using a MOMA sample

In this chapter, the single crystal rotation technique was applied to magnetically oriented microcrystal arrays (MOMAs) of cellobiose (monoclinic) microcrystals, and the principal values and principal axes of the chemical shift tensors of the C1 and C1′ carbons were determined. Rotation was performed about the magnetic χ_1, χ_2, and χ_3 axes of MOMA, and the measurements were performed at six different orientations with respect to the applied magnetic field. With this choice of rotation, crowded peaks were reduced and the peaks for the C1 and C1′ carbons were resolved by comparing with simulation results. Six components of the chemical shift tensor expressed with respect to the magnetic $\chi_1\chi_2\chi_3$-frame were determined. The tensors thus obtained were transformed into those relative to the molecular frame.

Chapter 4 Structure analysis of cellulose microfiber (Cotton, Ramie and Wood) via the anisotropic diamagnetic susceptibility

In this chapter, the orientational distribution of cellulose nanocrystals (CNCs) in a cellulose whisker (CW) was investigated by means of the X-ray diffraction of magnetically oriented samples of CWs. A cellulose sample (Cotton: Whatman CF11) was hydrolyzed and fractionated to prepare three different CW samples with a size

ranging from ca. 10 μm to 100 μm. Each of the fractions that were suspended in a liquid matrix was aligned under a static or a rotating magnetic field, and the matrix was solidified to prepare magnetically oriented microcrystal arrays (MOMAs). Then, the MOMAs were investigated by X-ray diffraction measurements. By analysis of the diffraction patterns, it is concluded that the c-axes of the CNCs are uniaxially distributed within a CW and that the orientational order increases with decreasing CW size. The average magnetic susceptibility $\langle \chi_a \rangle$ of the CWs was expressed in terms of their size and of the X-ray azimuthal half width. Using these expressions, a correlation length for the orientation of CNCs in a CW was determined. Then, this method developed by using Cotton CW was also applied to the Ramie and Wood CWs to determine the correlation lengths.

Chapter 5 Summary, Publication List and Acknowledgments

References

[1] Osullivan, A. C., *Cellulose* **1997,** *4* (3), 173-207; Klemm, D.; Heublein, B.; Fink, H. P.; Bohn, A., *Angewandte Chemie-International Edition* **2005,** *44* (22), 3358-3393; Habibi, Y.; Lucia, L. A.; Rojas, O. J., *Chemical Reviews* **2010,** *110* (6), 3479-3500.

[2] Moon, R. J.; Martini, A.; Nairn, J.; Simonsen, J.; Youngblood, J., *Chemical Society Reviews* **2011,** *40* (7), 3941-3994.

[3] Igarashi, K.; Uchihashi, T.; Koivula, A.; Wada, M.; Kimura, S.; Okamoto, T.; Penttila, M.; Ando, T.; Samejima, M., *Science* **2011,** *333* (6047), 1279-1282.

[4] Sugiyama, J.; Okano, T.; Yamamoto, H.; Horii, F., *Macromolecules* **1990,** *23* (12), 3196-3198; Sugiyama, J.; Persson, J.; Chanzy, H., *Macromolecules* **1991,** *24* (9), 2461-2466; Sugiyama, J.; Vuong, R.; Chanzy, H., *Macromolecules* **1991,** *24* (14), 4168-4175.

[5] Atalla, R. H.; Vanderhart, D. L., *Science* **1984,** *223* (4633), 283-285.

[6] Harris Robin K. , W. R. E., Duer Melinda J., NMR Crystallography. Wiley: 2009.

[7] Brouwer, D. H., Interplay between Solid-State NMR and Single-Crystal X-Ray Diffraction. eMagRes.: 2008.

[8] Nye, J. F., Physical properties of crystals : their representation by tensors and matrices. Clarendon Press: Oxford, 1985.

[9] Herbert, G., *Classical Mechanics*. Narosa Publishing House: 1997.

Chapter 2

Determination of ratio of diamagnetic anisotropy of cellobiose by X-ray diffraction measurement

2.1 Introduction

As introduced in Chapter 1, our laboratory has developed a technique to align the microcrystals 3-dimensionally under magnetic field to fabricate a magnetically oriented microcrystal array (MOMA). A MOMA facilitates the single-crystal X-ray analysis of microcrystalline powders [1-3] and single-crystal NMR study [4]. Information of diamagnetic anisotropy, $\chi_1 - \chi_2$ and $\chi_2 - \chi_3$ of crystal, which is a key parameter governing the orientation, is highly demanded in order to prepare composites having high degree of biaxial crystal alignment.

However, these information are available only for limited number of crystals.[5] We recently reported[6] a facile method for determination of the ratio of the anisotropic diamagnetic susceptibility $r_\chi = (\chi_2 - \chi_3)/(\chi_1 - \chi_2)$. It should be noted that $0 < r_\chi < \infty$. Although the absolute values of $\chi_1 - \chi_2$ and $\chi_2 - \chi_3$ affect both the orientation dynamics and the degree of alignment in equilibrium, only the ratio r_χ is sufficient to describe the degree of alignment against the thermal fluctuation in the final product.[7] In this method, the orientation distribution of magnetic axes in a composite is related to the broadening of its X-ray diffraction spots.

Cellobiose is usually used as the model substance for structural analysis of cellulose. We apply this method to the determination of the r_χ value of cellobiose crystal (monoclinic, space group $P2_1$, a=10.973Å, b=13.048Å, c=5.091Å, β=90.83°) [8] to evaluate the validity of the method and also pave the way for preparation of cellobiose MOMA.

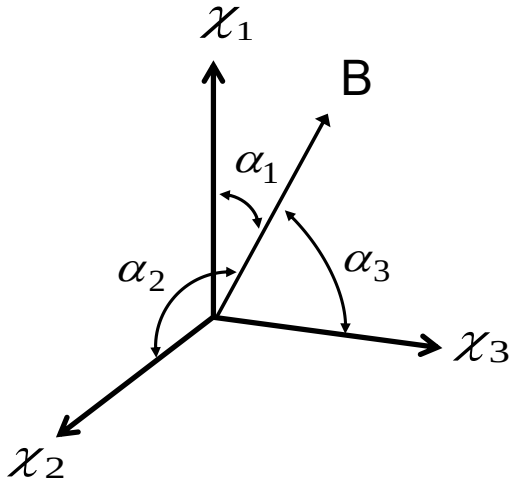

Fig. 1 Definition of angles α_1, α_2, and α_3, where χ_1, χ_2, and χ_3 are magnetic susceptibility axes and **B** is an applied magnetic field.

2.2 Theory

Let us assume that a crystal having three different diamagnetic susceptibilities χ_1, χ_2, and χ_3 is subjected to a magnetic field $\mathbf{B}$ whose axis makes angles α_1, α_2, and α_3 with respect to the axes of χ_1, χ_2, and χ_3, respectively (**Fig. 1**). Magnetic susceptibility χ_S in the direction of the axis of $\mathbf{B}$ is expressed as[9]

$$\chi_S = \sum_{i=1}^{3} \chi_i \cos^2 \alpha_i , \qquad (1)$$

where the subscript S indicates that the applied magnetic field is static. The magnetic energy in the vicinity of the stable alignment ($\chi_1 \| \mathbf{B}$) is expressed as a function of $a_2 \equiv \alpha_2 - \pi/2$ and $a_3 \equiv \alpha_3 - \pi/2$:

$$E_S = -\frac{VB^2 \chi_S}{2\mu_0} \approx \frac{VB^2}{2\mu_0}\left[(\chi_1 - \chi_2){a_2}^2 + (\chi_1 - \chi_3){a_3}^2\right], \qquad (2)$$

where isotropic and higher terms are disregarded, μ_0 is the magnetic permeability of vacuum, and V is the volume of the microcrystal. Using the Boltzmann distribution, $\exp(-E_S / k_B T)$, we evaluate the mean-square fluctuations in angles a_2 and a_3 as $< a_2{}^2 > = k_B T \mu_0 (VB^2)^{-1} (\chi_1 - \chi_2)^{-1}$ and $< a_3{}^2 > = k_B T \mu_0 (VB^2)^{-1} (\chi_1 - \chi_3)^{-1}$, respectively. Here, k_B and T are the Boltzmann constant and the absolute temperature, respectively.

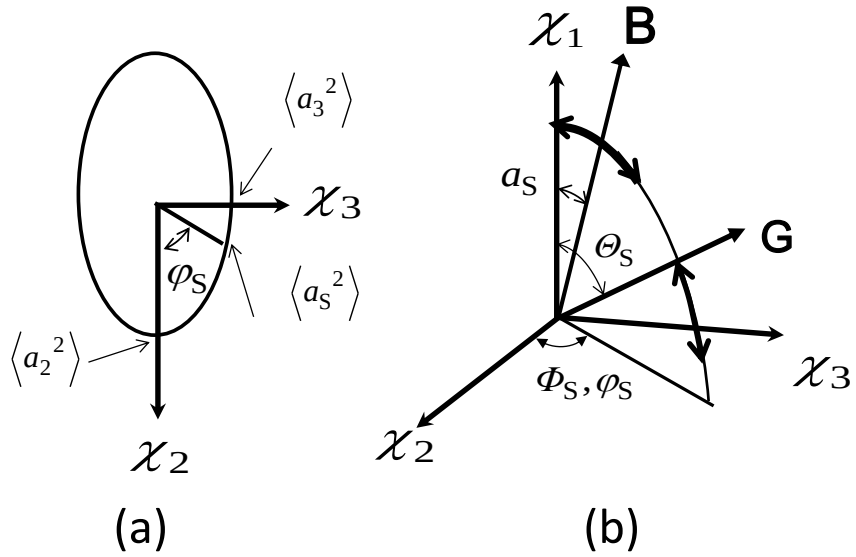

Fig. 2 (a) Fluctuation in the χ_1 axis viewed from the direction of magnetic field **B**. Mean-square amplitudes of fluctuation in the directions of χ_2 and χ_3 are $< a_2{}^2 >$ and $< a_3{}^2 >$, respectively, and that in the direction designated by φ_S is $< a_S{}^2 >$. (b) Amplitude of fluctuations in the reciprocal vector **G** is equal to that in the magnetic susceptibility axis χ_1 when χ_1, **B**, and **G** are all in the same plane. Reciprocal vector **G** is defined by the angles Φ_S and Θ_S with respect to the $\chi_1 \chi_2 \chi_3$ frame.

The fluctuation in the χ_1 axis viewed from the axis of $\mathbf{B}$ forms an ellipse because the energy E_S is a quadratic form in a_2 and a_3. The amplitudes of the mean-square fluctuation in the directions parallel to the χ_2 and χ_3 axes are $<a_2{}^2>$ and $<a_3{}^2>$, respectively [**Fig. 2(a)**]. Thus, the mean-square amplitude of the fluctuation in the direction designated by φ_S in **Fig. 2(a)** is expressed as

$$<a_S{}^2> = \frac{k_B T \mu_0 (VB^2)^{-1}}{\chi_1 - \chi_2 + (\chi_2 - \chi_3)\sin^2 \varphi_S} \quad . \qquad (3)$$

It is evident from eq. (3) that $<a_S{}^2>$ becomes $<a_2{}^2>$ and $<a_3{}^2>$ when $\varphi_S = 0$ and $\pi/2$, respectively.

Let us consider a reciprocal vector $\mathbf{G}(hkl)$ of a crystal, whose direction is defined by the angles Φ_S and Θ_S with respect to the $\chi_1\chi_2\chi_3$ frame [**Fig. 2(b)**]. Because the fluctuation in $\mathbf{G}$ is caused by the fluctuation in the χ_1 axis, the mean-square amplitude of the fluctuation in **G** is equal to $<a_S{}^2>$ if the angle Φ_S coincides with φ_S.

Because of the uniaxial nature of the magnetic field, the distribution of $\mathbf{G}$ is uniaxial about the direction of $\mathbf{B}$. Therefore, the orientation distribution of $\mathbf{G}$ forms a band of width $<a_S{}^2>^{1/2}$ on a reciprocal sphere with radius G. In **Fig. 3(a)**, the fluctuation band of $\mathbf{G}$ is shown with respect to the laboratory coordinates *xyz*. The direction of the *z* axis coincides with that of the axis of the magnetic field $\mathbf{B}$. Point *P*, at which the band intersects the Ewald sphere, is determined by angle Θ_S. At this point, the line of intersection is inclined with respect to the band by angle ξ_S, as shown in **Fig. 3b**. Therefore, the square of the band width, $H_S{}^2$, which is observed as a half-width in azimuthal plot of an X-ray diffraction spot, is obtained from the relation,

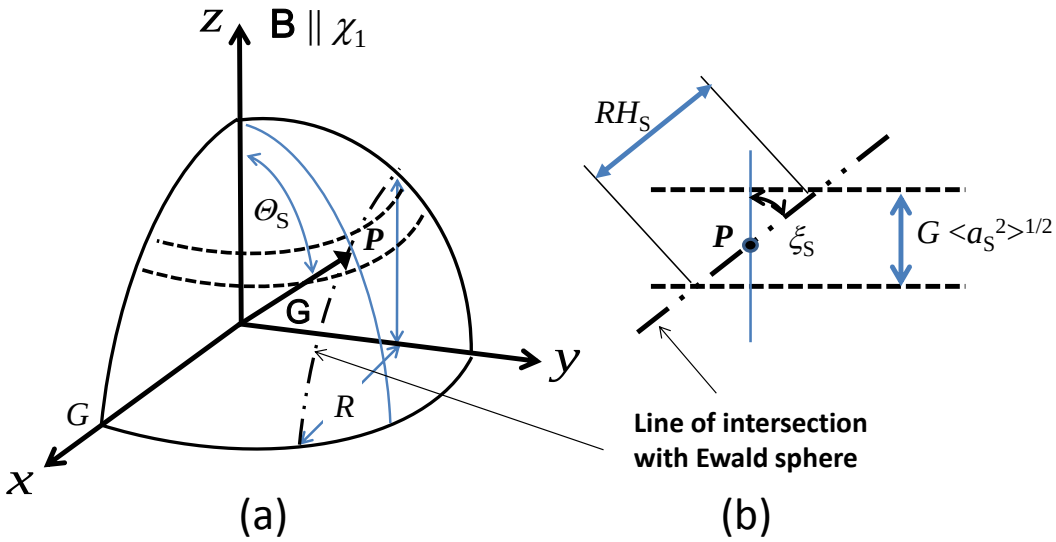

Fig. 3 (a) Band of the distribution of **G** vectors on the reciprocal sphere formed under a static magnetic field applied in the *z* direction. The band intersects with the Ewald sphere around point *P*. (b) Magnified view of the area around point *P*, showing the relationship between $<a_S^{\,2}>^{1/2}$ and the half-width H_S observed for the azimuthal plot in the X-ray diffraction pattern.

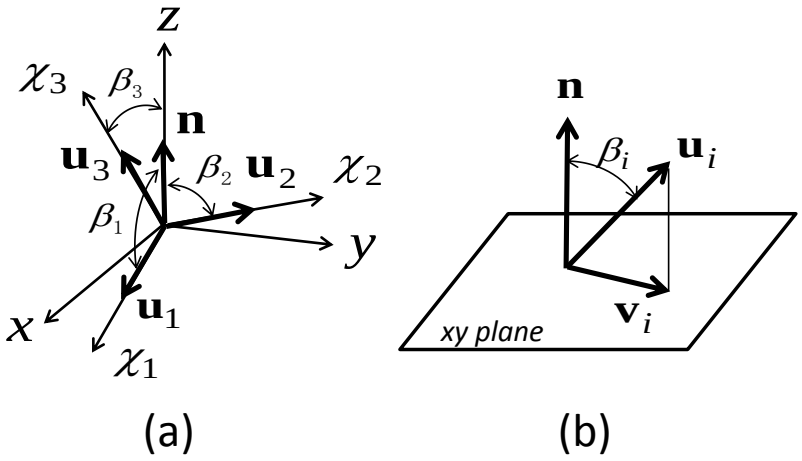

Fig. 4 (a) Unit vectors $\mathbf{u}_1$, $\mathbf{u}_2$, and $\mathbf{u}_3$ used for calculating the magnetic energy under a magnetic field rotating in the *xy* plane. Direction of the rotation axis **n** is defined by angles β_1, β_2, and β_3 with respect to unit vectors $\mathbf{u}_1$, $\mathbf{u}_2$, and $\mathbf{u}_3$. (b) Definition vectors $\mathbf{v}_i$ (i = 1,2,3).

$R^2 H_S{}^2 \cos^2 \xi_S = G^2 < a_S{}^2 >$, where $R^2 = G^2[1 - G^2/(4K^2)]$ is the square radius of the intersection circle of the Ewald sphere (radius *K*) and the reciprocal sphere (radius *G*). The quantity $\cos^2 \xi_S$ is determined as a function of *K*, *G*, and Θ_S. This approximation is valid when $< a_S{}^2 >$ is small. From eq. (3), we obtain

$$f_S{}^2 H_S{}^{-2} = \chi_1 - \chi_2 + (\chi_2 - \chi_3) \sin^2 \Phi_S, \qquad (4)$$

where

$$f_i{}^2 = \frac{k_B T \mu_0 m}{VB^2} \left[1 - \left(\frac{G}{2K \sin \Theta_i} \right)^2 \right]^{-1} \quad \text{with i = S or R} \qquad (5)$$

Here, i=S with Θ_S being the angle between the reciprocal vector $\mathbf{G}$ and the χ_1 axis, as shown in **Fig. 2b**. The factor m is unity for i=S and m=2 for i=R.

Next, we consider the fluctuations under a rotating magnetic field. Let us define a magnetic field $\mathbf{B} = (B\cos\omega t, B\sin\omega t, 0)$ rotating in the *xy* plane and a unit vector $\mathbf{n}$ parallel to the *z* axis. We define unit vectors $\mathbf{u}_1$, $\mathbf{u}_2$, and $\mathbf{u}_3$ as parallel to the χ_1, χ_2, and χ_3 axes, respectively. The direction cosines of $\mathbf{n}$ with respect to $\mathbf{u}_1$, $\mathbf{u}_2$, and $\mathbf{u}_3$ are defined as $\cos\beta_1$, $\cos\beta_2$, and $\cos\beta_3$, respectively (**Fig. 4**). The projection of $\mathbf{u}_i$ (*i* = 1, 2, 3) on the *xy* plane is expressed as $\mathbf{v}_i = \mathbf{u}_i - \mathbf{n}\cos\beta_i$. Thus, the magnetic energy is given by

$$E_R = -\frac{V}{2\mu_0} \sum_{i=1}^{3} \chi_i (\mathbf{B} \cdot \mathbf{u}_i)^2 = -\frac{V}{2\mu_0} \sum_{i=1}^{3} \chi_i (\mathbf{B} \cdot \mathbf{v}_i)^2 = -\frac{VB^2}{2\mu_0} \sum_{i=1}^{3} \chi_i \sin^2 \beta_i \cos^2(\omega t + \delta_i), \qquad (6)$$

where δ_i is the phase of $\mathbf{v}_i$ and the subscript R indicates that the applied magnetic field is rotating. If the magnetic field rotates at a high speed such that the change in the directions of the magnetic axes is negligible in a single rotation, then $\cos^2(\omega t + \delta_i)$ is time averaged over one rotation to give a factor of 1/2. Thus, the magnetic energy in the vicinity of the stable alignment ($\chi_3 \| \mathbf{n}$) is expressed as a function of $b_1 \equiv \beta_1 - \pi/2$ and $b_2 \equiv \beta_2 - \pi/2$:

$$E_{\mathrm{R}} \approx \frac{VB^2}{4\mu_0}\left[(\chi_1 - \chi_3){b_1}^2 - (\chi_2 - \chi_3){b_2}^2\right], \qquad (7)$$

where isotropic and higher terms are disregarded. Similar to the case of the static magnetic field, the mean-square fluctuations in the χ_3 axis in the direction designated by φ_{R} in **Fig. 5** is expressed as

$$< {b_{\mathrm{R}}}^2 > = \frac{2k_{\mathrm{B}}T\mu_0 (VB^2)^{-1}}{\chi_1 - \chi_3 - (\chi_1 - \chi_2)\sin^2 \varphi_{\mathrm{R}}} . \qquad (8)$$

We find that $< {b_{\mathrm{R}}}^2 >$ becomes $< {b_1}^2 > = 2k_{\mathrm{B}}T\mu_0 (VB^2)^{-1}(\chi_1 - \chi_3)^{-1}$ and $< {b_2}^2 > = 2k_{\mathrm{B}}T\mu_0 (VB^2)^{-1}(\chi_2 - \chi_3)^{-1}$ when $\varphi_{\mathrm{R}} = 0$ and $\pi/2$, respectively. Further,

$${f_{\mathrm{R}}}^2 {H_{\mathrm{R}}}^{-2} = \chi_1 - \chi_3 - (\chi_1 - \chi_2)\sin^2 \Phi_{\mathrm{R}} , \qquad (9)$$

where ${f_{\mathrm{R}}}^2$ is determined using eq. (5), with $\Theta_{\mathrm{i}} = \Theta_{\mathrm{R}}$. Here, Θ_{R} is the angle between the reciprocal vector **G** and the χ_3 axis, as shown in **Fig. 5**.

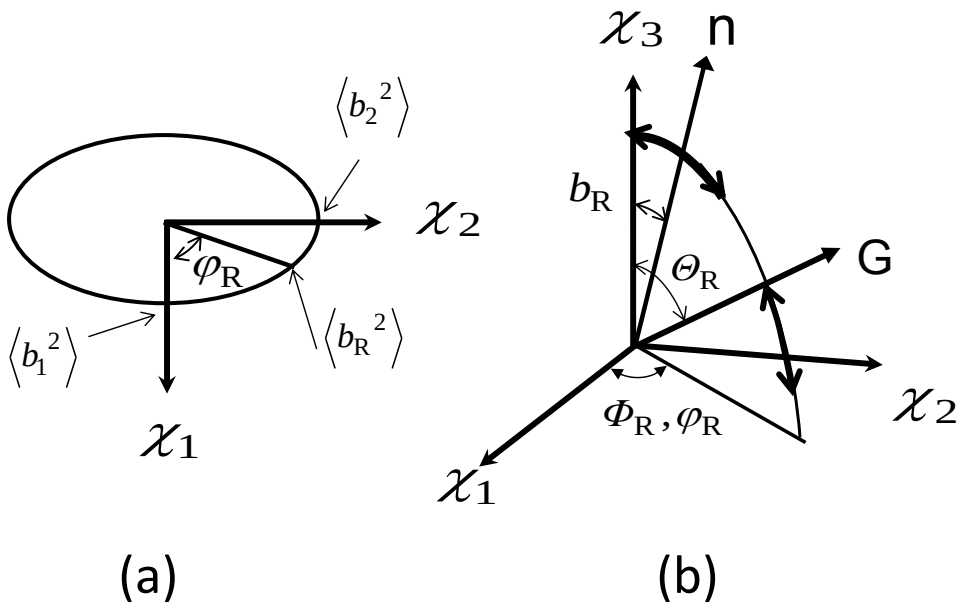

Fig. 5 (a) Fluctuation in the χ_3 axis viewed from the direction **n** perpendicular to the rotating magnetic field. Mean-square amplitudes of fluctuation in the directions of χ_1 and χ_2 are $<b_1^2>$ and $<b_2^2>$, respectively, and that in the direction designated by φ_R is $<b_R^2>$. (b) Amplitude of fluctuations in the reciprocal vector **G** is equal to that in the magnetic susceptibility axis χ_3 when χ_3, **n**, and **G** are all in the same plane. Reciprocal vector **G** is defined by the angles Φ_R and Θ_R with respect to the $\chi_1\chi_2\chi_3$ frame.

We observe that the plot of the quantity on the left-hand side of eq. (4) as a function of $\sin^2 \Phi_S$ forms a line whose *y* intercept and slope are equal to those of $\chi_1 - \chi_2$ and $\chi_2 - \chi_3$, respectively [**Fig. 6(a)**]. This plot can be generated as follows: because the

susceptibility axes χ_1, χ_2, and χ_3 are related to the crystallographic axes *a*, *b*, and *c*,[10] the angle Θ_S [**Fig. 2(b)**] is determined for a given reciprocal vector **G**(*hkl*). Thus, the factor f_i^2 in eq. (5) is determined if the values of V, B, and T are given. Consequently, the quantity on the left-hand side of eq. (4) can be determined using the experimental value of half-width H_S corresponding to **G**(*hkl*). Because the angle Φ_S [**Fig. 2(b)**] is also determined for **G**(*hkl*), we can complete the plot. In many cases, the crystal volume V (or the average volume of the microcrystalline powder) is unknown. In these cases, we can generate a plot with the front factor $k_B T\mu_0/(VB^2)$ of f_i^2 being set equal to unity so that we only obtain the ratio $(\chi_1-\chi_2)/(\chi_2-\chi_3)$ from the intercept and slope values instead of the absolute values. Based on eq. (9), the same procedure can be performed using the experimental data obtained under the rotating magnetic field [**Fig. 6(b)**]. From this plot, $\chi_1-\chi_3$ and $\chi_1-\chi_2$ are determined. If the crystal volume V (or the average volume of the microcrystalline powder) is unknown, only the ratio $(\chi_1-\chi_3)/(\chi_1-\chi_2)$ is determined.

In conclusion, we have proposed a facile method to determine the anisotropic diamagnetic susceptibilities of a microcrystalline powder of biaxial crystals by performing X-ray diffraction measurements. The experiment can be performed by *in-situ* X-ray measurement of a magnetically oriented microcrystalline suspension (MOMS) [11] or *ex-situ* X-ray measurement of a magnetically oriented microcrystalline array (MOMA) [3] prepared under a static or rotating magnetic field.

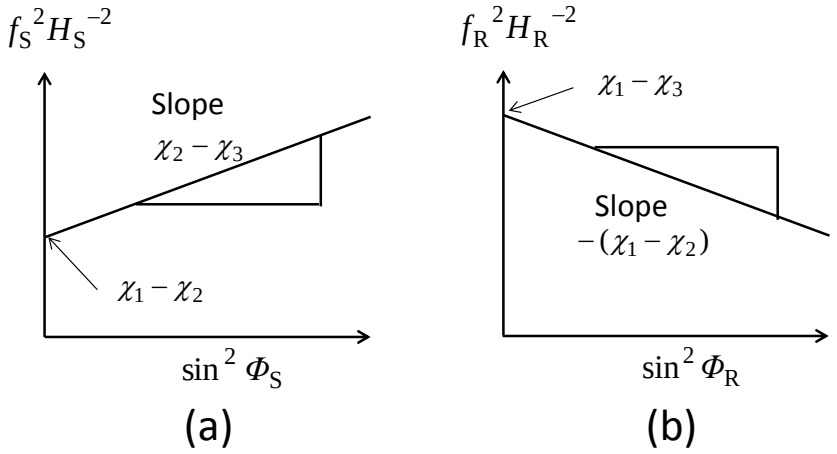

Fig. 6 Determination of the anisotropic diamagnetic susceptibilities under (a) static and (b) rotating magnetic fields.

2.3 Experiement

As-received cellobiose crystal sample (supplied from Matsutani Chemical Industry Co. Ltd) was pulverized using a mortar and pestle, and dispersed in UV (ultraviolet)-curable monomer (XVL-14 of Kyoritsu Chemical and Co. Ltd). The concentration of the crystallites was ca. 17 wt%. The suspension was allowed to stand for a few days to form a lower layer of large crystallites and an upper layer of small ones. A small amount of the suspension was collected from between these two layers using a pipette and was poured into two plastic containers (diameter, 5 mm; height, ca. 8mm). The actual concentration may therefore be less than 17 wt%.

One suspension was exposed to a static magnetic field of 8 T (a Sumitomo Heavy Industry cryocooler-cooled superconducting magnet) for 1.5 h and then irradiated with UV light for 3 h, with the magnetic field being applied, to photopolymerize the monomer and consolidate the alignment [**Fig. 7(a)**, referred to as static-sample]. Under this experimental condition, the easy magnetization axis χ_1 aligns uniaxially parallel to the

applied magnetic field, giving rise to a fiber diffraction pattern ($\chi_1 \parallel$ fiber axis). The other was rotated at 40 rpm in a static magnetic field of 8 T for 3 h with the rotation axis being perpendicular to the field. Then, the UV light was irradiated for 3 h, with the magnetic field and the rotation being applied, to photopolymerize the monomer [**Fig. 7(b)**, referred to as rotating-sample]. Under this experimental condition, the hard magnetization axis χ_3 aligns uniaxially in the direction of sample rotating axis, giving rise to a fiber diffraction pattern ($\chi_3 \parallel$ fiber axis).

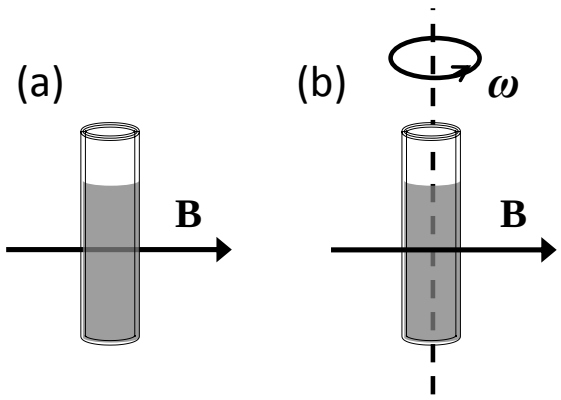

Fig. 7 Sample preparation. (a) static-sample: the suspension was placed under a static magnetic field **B** and irradiated with UV light to consolidate the alignment. (b) rotating-sample: the suspension was rotated in a static magnetic field at a rotating speed of ω and irradiated with UV light to consolidate the alignment.

X-ray diffraction measurement was performed for 40 min using an MAC Science Dip 2000 diffractometer equipped with an MXP18HF22 rotating anode generator (45 kV, 84 mA). Graphite-monochromated Cu Kα radiation was used ($\lambda = 1.54078$ Å; wave number $K = 2\pi / \lambda = 4.078$ Å^{-1}). The collimator size was 0.9 mmϕ. The crystal-to-detector distance was 150.0 mm. The divergence of the X-ray beam was 0.5°.

2.4 Results and discussion

Due to the Brownian motion of microcrystals suspended in a liquid medium, fluctuation in magnetic axes that are embedded in crystal occurs when the microcrystals are subjected to a magnetic field. This fluctuation is anisotropic because of the diamagnetic anisotropy of crystal, resulting in anisotropic fluctuation in crystallographic axes. In the theory part, we derived the relationship between the amplitude of the fluctuation in magnetic axes and the half width of X-ray diffraction spots resulting from the fluctuation in crystallographic axes. The half width H_S of the diffraction spot, corresponding to the (*hkl*) plane, obtained from the sample with uniaxial χ_1 alignment (a static-sample in the present case) is related to the magnetic susceptibilities by the following equation:

$$\frac{{f_S}^2}{{H_S}^2} = \chi_1 - \chi_2 + (\chi_2 - \chi_3)\sin^2 \Phi_S , \qquad (1)$$

where f_S is a correction factor expressed as

$${f_S}^2 = \frac{k_B T \mu_0}{VB^2}\left[1 - \left(\frac{G}{2K\sin\Theta_S}\right)^2\right]^{-1} . \qquad (2)$$

Here, Φ_S and Θ_S are the angles characterizing the direction of the reciprocal vector **G**(*hkl*) relative to the $\chi_1\chi_2\chi_3$ frame as shown in **Fig. 8(a)**, and μ_0, magnetic permeability of vacuum; k_B, Boltzmann constant; T, temperature; V, volume of a microcrystal; B, applied magnetic flux density; G, length of the reciprocal vector for

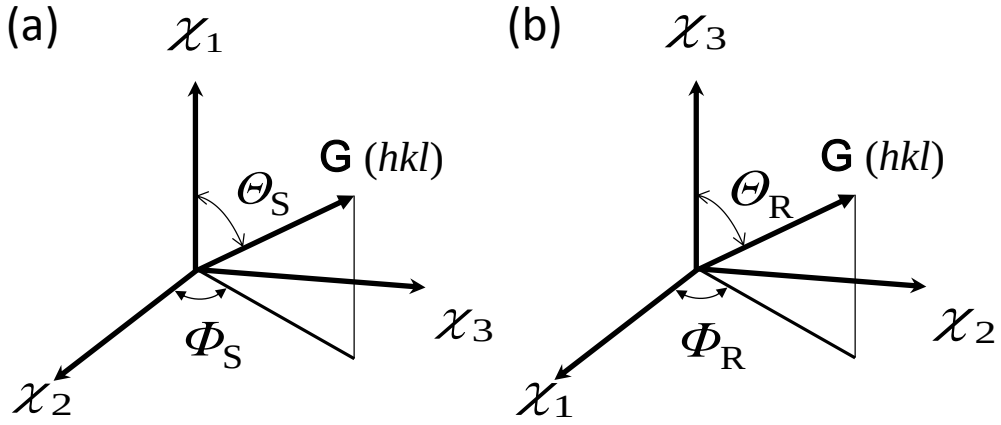

Fig. 8 Angles Θ and Φ characterizing the direction of the reciprocal vector $\mathbf{G}(hkl)$ with respect to the $\chi_1\chi_2\chi_3$ coordinates. (a) in the case of a static-sample and (b) in the case of a rotating sample. Suffices S and R indicate “static” and “rotating”, respectively.

the crystal plane (*hkl*) under consideration; K, radius of Ewald sphere, equal to the wave number of the X-ray. We find from eq. (1) that the left-hand side quantity $f_S{}^2 H_S{}^{-2}$ linearly depends on $\sin^2 \Phi_S$, giving rise to the slope of $\chi_2 - \chi_3$ and the intercept of $\chi_1 - \chi_2$. Arbitrariness of the value of f_S is inevitable when the value of the volume *V* of microcrystals is unavailable, and hence the determination of the absolute values of $\chi_2 - \chi_3$ and $\chi_1 - \chi_2$ cannot be made. However, it is possible to determine the ratio $r_\chi = (\chi_2 - \chi_3)/(\chi_1 - \chi_2)$ by assigning an arbitrary value to the factor of $k_B T\mu_0 /(VB^2)$ in f_S. In the present experimental analysis, we set this factor equal to unity.

A similar equation is given for the half width H_R of the sample with uniaxial χ_3

alignment (case rotating-sample in the present) by the following equation:

$$\frac{{f_{\mathrm{R}}}^2}{{H_{\mathrm{R}}}^2} = \chi_1 - \chi_3 - (\chi_1 - \chi_2)\sin^2 \Phi_{\mathrm{R}}\,, \qquad (3)$$

where f_{R} is a correction factor expressed as

$${f_{\mathrm{R}}}^2 = \frac{2k_{\mathrm{B}}T\mu_0}{VB^2}\left[1-\left(\frac{G}{2K\sin\Theta_{\mathrm{R}}}\right)^2\right]^{-1}. \qquad (4)$$

Here, Φ_{R} and Θ_{R} are the angles characterizing the direction of the reciprocal vector **G**(*hkl*) relative to the $\chi_1\chi_2\chi_3$ frame as shown in **Fig. 8(b)**.

Now we need to locate the magnetic axes with respect to the crystallographic axes using the X-ray diffraction pattern in order to evaluate the angles Φ_{R} and Θ_{R}. **Figures 9(a)** and **(b)** show the X-ray diffraction patterns obtained from the sample prepared under static- and rotating magnetic fields, respectively. Symmetry axes in the figure are the χ_1 and χ_3 axes, respectively.

In Fig. 9(b), the vertical direction coincides with the χ_3 axis. Because the cellobiose crystal belongs to the monoclinic crystal system, the two-fold crystal axis (here the *b* axis) is one of the magnetic susceptibility axes.[10] Thus, we conclude $\chi_3 \| b$ (also $\chi_3 \| b^*$, with asterisk indicating reciprocal vector). The assignment of diffraction spots in **Fig. 9(b)** by their 2θ values is consistent with this conclusion.

Because (i) the reciprocal a^*c^* plane is perpendicular to the b^* axis, (ii) the $\chi_1\chi_2$ plane is perpendicular to the χ_3 axis, and (iii) $\chi_3 \| b^*$, the χ_1 and χ_2 axes are on

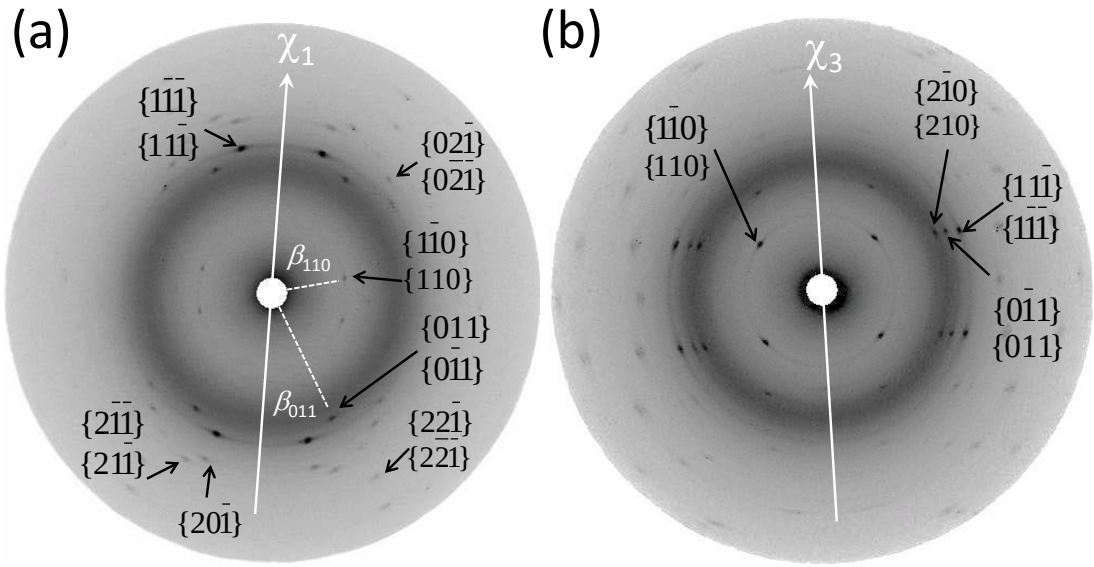

Fig. 9 X-ray diffraction patterns of (a) static-sample and (b) rotating-sample. The assignment for the diffraction spots {*hkl*}s used for the analyses is indicated. The directions of the χ_1 and χ_3 axes are shown in figures (a) and (b), respectively. The angles β_{110} and β_{011} used to determine the a^* and c^* axes with respect to the χ_1 axis (see Fig. 4) is shown in fig. (a).

the a^*c^* plane [**Fig. 10**]. Using the diffraction spots for {110} and {011} planes in **Fig. 9(a)**, we locate the χ_1 and χ_2 axes relative to the a^* and c^* axes. We define the angle of the diffraction spot {110} on the diffraction image with respect to the χ_1 axis as β_{110} [**Fig. 9(a)**] and the angle of the reciprocal a^* axis with respect to the χ_1 axis as α^* [**Fig. 10**]. By the diffraction law, α^* is related to β_{110}. Next, we define the angle for the diffraction spot {011} on the diffraction image with respect to the χ_1 axis as β_{011} [**Fig. 9(a)**] and the angle of the reciprocal c^* axis with respect to the χ_1 axis

as γ^* [**Fig. 10**]. Then, γ^* is related to β_{011}. Using the experimental data, β_{110}=73.2° and β_{011}=29.5°, we obtain α^*=67.9° and γ^*=22.8°. From this result, the a^* and c^* axes are located on the $\chi_1\chi_2$ plane as shown in **Fig. 10**. This assignment consistently explains the positions of other diffraction spots in **Fig. 9(a)**.

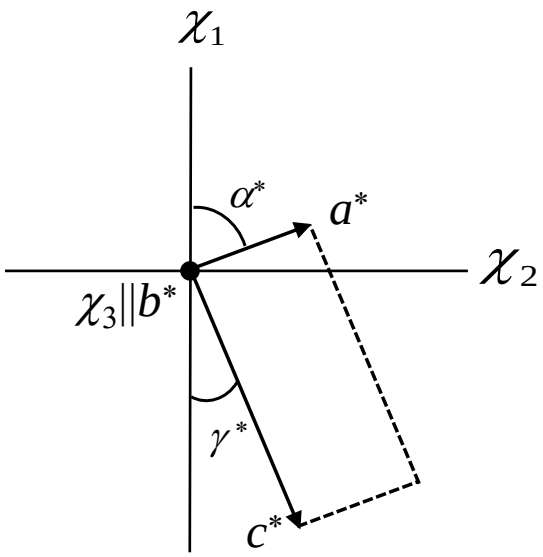

Fig. 10 The direction of the a^* and c^* axes with respect to the χ_1 axis, characterized by the angles α^*=67.9° and γ^*=22.8°. Using this relation, the angles Θ and Φ in Fig. 2 are determined.

Azimuthal β-scans were performed on diffraction spots for the $\{110\}$, $\{1\bar{1}0\}$; {011}, $\{0\bar{1}1\}$; $\{1\bar{1}1\}$, $\{\bar{1}\bar{1}1\}$; $\{02\bar{1}\}$, $\{0\bar{2}\bar{1}\}$; $\{20\bar{1}\}$; $\{2\bar{1}1\}$, $\{2\bar{1}\bar{1}\}$; $\{22\bar{1}\}$, $\{2\bar{2}\bar{1}\}$ planes in **Fig. 9(a)** obtained for the static-sample, and their half widths were determined. The results are summarized in Table I. Similar analysis was performed for the X-ray diffraction spots for the {110}, $\{1\bar{1}0\}$; {210}, $\{2\bar{1}0\}$; {011}, $\{0\bar{1}1\}$; $\{1\bar{1}1\}$, $\{\bar{1}\bar{1}1\}$ planes shown in **Fig. 9(b)** obtained for the rotating-sample. The results are also summarized in Table I. In most cases, four diffraction spots (Peaks 1, 2, 3, and 4) appear. This is due to the crystal

	$\{hkl\}$	2θ /deg	G /deg	Θ /deg	Φ /deg	f^2	H /deg					f^2/H^2 /deg^{-2}
							Peak 1	Peak 2	Peak 3	Peak 4	Average	
Static	{110} {1$\bar{1}$0}	10.6	0.75	107	42.2	1.01	3.15	3.54	3.81	3.27	3.44	0.0853
	{011} {0$\bar{1}$1}	18.8	1.33	30.8	45.1	1.11	1.83	2.27	2.37	2.2	2.17	0.236
	{1 1 $\bar{1}$} {1$\bar{1}\bar{1}$}	20.3	1.44	160	84.0	1.38	2.52	2.1	1.48	2.42	1.86	0.398
	{02$\bar{1}$} {0$\bar{2}\bar{1}$}	22.2	1.57	137	-63.5	1.09	2.38	1.82	2.22	2.05	2.12	0.242
	{20$\bar{1}$}	23.5	1.66	160	0	1.53	3.07	2.87	2.7	2.8	2.86	0.187
	{2 1 $\bar{1}$} {2$\bar{1}\bar{1}$}	24.5	1.73	154	39.6	1.32	2.79	2.22	2.58	2.4	2.5	0.211
	{22$\bar{1}$} {2$\bar{2}\bar{1}$}	27.3	1.92	144	58.6	1.20	2.05	2.08	1.94	2.08	2.04	0.287
Rotating	{110} {1$\bar{1}$0}	10.6	0.75	49.9	-68.0	2.03	3.12	3.49	3.31	3.01	3.23	0.195
	{210} {2$\bar{1}$0}	17.6	1.25	67.2	-68.0	2.06	2.97	3.27	3.22	3.6	3.27	0.192
	{011} {0$\bar{1}$1}	18.8	1.33	68.8	22.8	2.06	2.03	2.36	4.04	1.81	2.56	0.315
	{1 1 $\bar{1}$} {1$\bar{1}\bar{1}$}	20.3	1.44	70.5	-2.16	2.07	2.27	2.08	3.8	2.6	2.7	0.284

Table I The experimental results for the half width H for {hkl} planes. The calculated results for the angles Θ and Φ characterizing the direction of the reciprocal **G** are shown. Quantity f is the correction factor (eqs. (2) and (3)). Plots of f^2/H^2 as a function of $\sin^2\Phi$ is shown in Figs. 5(a) and (b).

symmetry and the symmetry about the magnetic axis. Ideally, the half widths of these four spots are equal, but we observed scattering of the values of the half widths as seen in Table I. A poor signal-to-noise ratio of the diffraction data and an imperfect setting of the sample (the magnetic axis slightly deviates from being perpendicular to the X-ray beam, etc.) might be responsible for the unequal half width values.

In **Figs. 11(a) and (b)**, H-Φ plots (eqs. (1) and (3)) for the static- and rotating-samples, respectively, are shown. Here we set $k_B T\mu_0/(VB^2)=1$ by the reason previously mentioned. **From Fig. 11(a)**, we obtain $r_\chi = 1.7$, and from **Fig. 11(b)**, we obtain $(\chi_1-\chi_3)/(\chi_1-\chi_2)=2.3$, leading to $r_\chi = 1.4$. Ideally, these two

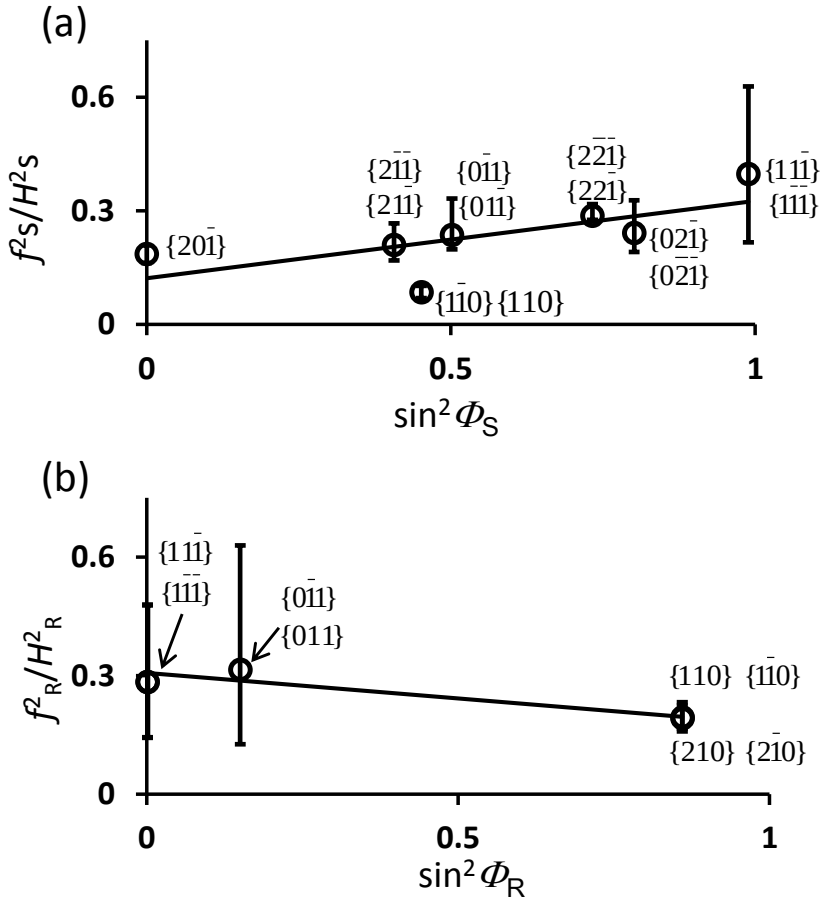

Fig. 11 Squared inverse of the half widths are plotted as a function of $\sin^2\Phi$. Figures (a) and (b) are the plots for the static- and rotating samples, respectively. Suffices S and R indicate the static and rotating, respectively. From the slope of the line and the value of the intercept with the vertical axis, the ratio r_χ is determined using eqs. (1) and (3).

values should coincide. The discrepancy might come from the insufficient data quality. In order to improve the data quality, we might need the correction of the sample shape and size with respect to the collimator size, the correction of the X-ray beam divergence, the exact setting of the magnetic axis of the sample with respect to the X-ray beam, the estimation of the 2θ-dependence of the half width, etc.

2.5 Conclusion

In conclusion, we determined the ratio r_χ of the diamagnetic anisotropy of cellobiose crystal by using X-ray diffraction measurement. We first determined the directions of the magnetic axes with respect to the crystallographic axes. We found that χ_3 is parallel to the b^* axis and the χ_1 axis makes angles of 67.9° and 22.8° with respect to the a^* and c^* axes, respectively. The half widths of the (*hkl*) diffraction spots exhibited dependence on the angles Φ and Θ characterizing the direction of the reciprocal vector **G**(*hkl*) with respect to the frame of the magnetic axes, from which the ratio r_χ of the diamagnetic anisotropy was determined by the method reported previously. From the plot, we determined r_χ =1.4~1.7. Although the experimental result is sensitive to the sample quality and X-ray measurements, the method presented here will be useful to determine crystal diamagnetic anisotropy from a microcrystalline powder.

References

[1] Kimura, T.; Chang, C.; Kimura, F.; and Maeyama, M. *J. Appl. Cryst.* **2009**, 42, 535-537.

[2] Kimura, F.; Kimura, T.; Oshima, W.; Maeyama, M.; and Aburaya, K. *J. Appl. Cryst.* **2010**, 43, 151-153.

[3] Kimura, F.; Mizutani, K.; Mikami, B.; and Kimura, T. *Cryst. Growth Des*. **2011**, 11, 12-15.

[4] Kusumi, R.; Kimura, F.; Song, G.; and Kimura, T. *J. Magn. Reson.*, **2012**, 223, 68-72.

[5] Gupta, R. R; "Landolt-Bornstein", Hellwege, H.-H; and Hellwege, A. W. Eds., Springer Verlag, Berlin, 1986, vol.II/16, Chapt.8.

[6] Kimura, T.; Song, G.; Matsumoto, K.; Fujita, K.; and Kimura, F. *Jpn. J. Appl. Phys*. **2012**, 51, 040202.

[7] Kimura, T. Jpn. *J. Appl. Phys.* **2009**, 48, 020217

[8] Chu, S. S. C.; Jeffrey, G. A. *Acta Cryst.* **1968**, B24, 830-838.

[9] Weiss, A. and Witte, H.: in Magnetochemie (Verlag Chemie, Weinheim, 1973) Chap. 3. (Japanese translation, Misuzu Shobo, Tokyo, 1980).

[10] Nye, J. F. in Physical Properties of Crystals (Clarendon Press, Oxford, 1985) Chap. 1.

[11] Matsumoto, K.; Kimura, F.; Tsukui, S. and Kimura, T. *Cryst. Growth Des.* **2011**, 11, 945-948.

Chapter 3

A single crystal NMR approach for determining chemical shift tensors from powder samples via magnetically oriented microcrystal arrays

3.1 Introduction

The chemical shift tensor (CST) of a nucleus is very sensitive to electronic structure around the nucleus in a crystal. Chemical shift tensor reflects the full local structural information around the resonance nuclei. For a complete characterization of the CST, it is expressed by three principal values and directions of the principal axes with respect to a crystal coordinate system.

Single crystal NMR is a direct method to determine the chemical shift tensor with highest accuracy.[1, 2]

Powder solid state NMR measurement gives rise to isotropic chemical shifts with magic angle spinning (MAS), or three principal values without MAS. However, single crystal NMR measurement obtains a complete chemical shift tensor.

Single-crystal NMR measurement can determine the chemical shift tensor directly and precisely. Currently, many techniques have been developed to determine the three principal values. Therefore, most of the chemical shift tensor data reported is only principal values. However, very few reports are about determining the orientation of magnetic axes effectively. Till now, single crystal NMR is the most effective method to determine the full chemical shift tensor. Limitation: a single crystal with suitable size is needed (mm scale). However, this single crystal is not commercially available. In most cases, very much efforts and time are taken to recrystallize some crystals.

As mentioned in Chapter 1, we recently showed that a magnetically oriented

microcrystal array (MOMA) is a resin composite in which microcrystals are aligned three-dimensionally, and it behaves like a single crystal in single crystal NMR or X-ray diffraction measurement.[3, 4]

In Chapter 2, magnetic anisotropy of cellobiose has been determined successfully. In this chapter, MOMA of cellobiose was then prepared and single crystal NMR measurement was performed on this MOMA. Complete chemical shift tensors of C1 and C1` were determined, combined with a 2D NMR technique. Then, the result was discussed based on the local molecular symmetry.

3.2 Experiment

Cellobiose MOMA samples were prepared following the method reported previously.[5] As-received cellobiose crystals (Wako Pure Chemical Industries, Ltd.) were pulverized with a mortar and passed through a 125/90 μm mesh and 75/50 μm mesh consecutively, then the fraction of a powder on the 75/50 μm -mesh was collected. The obtained microcrystalline powder was dispersed in a UV-curable monomer (POLY201 of Arakawa Chemical Industries, Ltd.; viscosity of 5 Pa s). The weight fraction of microcrystals was ca. 0.2.

The obtained suspension was poured into a plastic tube of 4-mm diameter and ca. 15-mm height. The tube was then mounted on a sample-rotating unit placed in the bore center of a Sumitomo Heavy Industry cryogen-free superconducting magnet generating an 8-T static horizontal magnetic field. The sample rotation axis was vertical (the *z*-axis) and the tube axis was set horizontal or vertical. Three kinds of rod-shaped MOMA samples, M1, M2, and M3, were prepared, where the rod axes (tube axes) were parallel to (M1) χ_3 axis; (M2) χ_1 axis; (M3) χ_2 axis. Here we define $\chi_1 > \chi_2 > \chi_3$. Two different frequencies of rotation were applied within one revolution: the

rotation frequency was switched between ω=10 and ω=80 rpm every 90°. After 70 min of this frequency-modulated rotation of the tube, the suspension was irradiated with UV light for 45 min to photopolymerize the UV-curable monomer. Then, the consolidated specimen was removed from the tube to obtain a rod-shaped cellobiose MOMA (ca. 3 mm in diameter and 10 mm in height) for NMR measurements.

The three-dimensional alignment of the cellobiose microcrystals in the MOMA sample was confirmed using X-ray diffraction. X-ray diffraction data were collected on a Rigaku RAXIS RAPID II system equipped with an imaging plate using graphite-monochromatized Cu Kα radiation. The collimator size and crystal-to-detector distance were 0.5 mmϕ and 127 mm, respectively. Data were collected via ω scans from −15° to 15° at ambient temperature.

^{13}C CP solid-state NMR measurements under proton decoupling were performed using a probe with a goniometer (sample rotation axis (rod axis) is perpendicular to the applied magnetic field $\mathbf{B}_0$) at ambient temperature (20 °C) with a JEOL ECA-500 system operated at a ^{13}C resonance frequency of 125 MHz. Recycle delay and contact time are 60 s and 2 ms, respectively. Total scans of 600~2160 were taken. The SUPER experiment [6] was performed on a Varian 400 spectrometer operating at 100 MHz for ^{13}C using a 4 mm zirconia rotor spinning at 3 kHz. Recycle delay, total scans, contact time and complex points for 2D increments were 9 s, 4096, 2 ms, and 16, respectively. MAS measurement was performed on a Varian 400 spectrometer operating at 100 MHz for ^{13}C using a 4 mm zirconia rotor spinning at 15 kHz. Recycle delay, total scans, and contact time were 120 s, 256, and 2 ms. Chemical shifts for all measurements were referred to adamantane (ADM).

3.3 Results and discussion

3.3.1 X-ray diffraction pattern

Fig. 1 shows the X-ray diffraction patterns of the obtained cellobiose MOMA sample (sample M2). The sample clearly shows well-separated diffraction spots in the diffraction images taken from the direction of the χ_1, χ_2, and χ_3 axes. The half widths in the azimuthal plot were ca. 5° for most of the spots in all of the images in the figure. This result indicates that the microcrystals in the polymer matrix are aligned three-dimensionally. The same order of orientations was confirmed for the other two MOMA samples (M1 and M3).

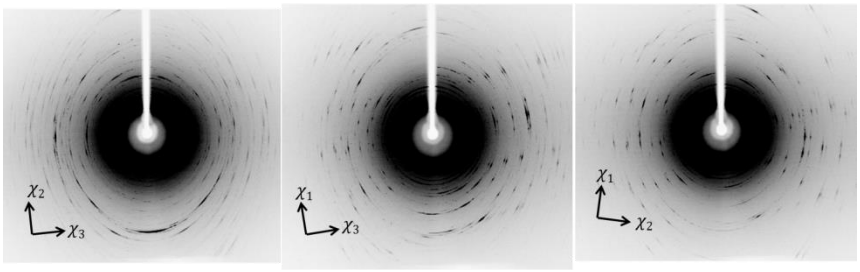

Fig. 1 X-ray diffraction images of a MOMA (sample M2) taken from three different directions. Sharp spots indicate three-dimensional orientation of the microcrystals in MOMA. χ_1, χ_2, and χ_3 indicate the directions of the magnetic axes.

3.3.2 Theoretical background

3.3.2.1 Crystal symmetry

Cellobiose crystals belong to monoclinic system (space group $P2_1$, Z=2, a=5.0633 Å, b= 13.017 Å, c=10.9499 Å, β=90.811º).[7] In the monoclinic crystals, the two-fold rotation or inversion axis coincides with one of three magnetic axes.[8] We reported previously [9] that the b axis (two-fold rotation axis) corresponds to the hard

magnetization axis χ_3 in cellobiose crystals. The other two magnetic axes χ_1 (easy magnetization axis) and χ_2 (intermediate axis) are located on the *ac* plane. The relationship between magnetic χ_1 and χ_2 axes and crystallographic *a* and *c* axes has been reported in our previous work [5, 10] and shown in **Fig. 2**. There are two identical molecules in the unit cell, which are related by a two-fold screw axis. We designate these two molecules by A_1(*lmn*) and A_2(*-l-mn*), where (*lmn*) indicates the direction cosines with respect to the χ-frame.

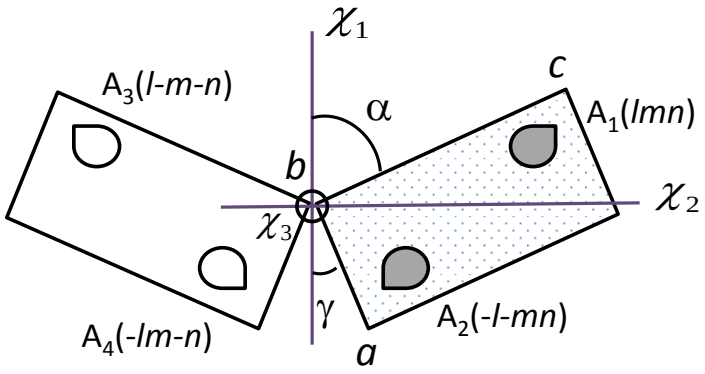

Fig. 2 Unit cell of cellobiose crystals and twin structure that occurs in a MOMA sample. There are two identical molecules with different orientations in a unit cell, designated by A_1(*lmn*) and A_2(*-l-mn*), where (*lmn*) indicates the direction cosines with respect to χ-frame. In a MOMA, another orientation (twin) that is produced by a π rotation of the unit cell about the χ_1 (or χ_2) axis is allowed. The orientations of the molecules in the twin are designated by A_3(*l-m-n*) and A_4(*-lm-n*). The direction of the χ_1 axis with respect to the *c* and *a* axes are α =67.2° and γ =21.8°, respectively.

3.3.2.2 Twin structure

The magnetic axes, χ_1, χ_2, and χ_3, of each microcrystal are aligned three-dimensionally in a MOMA. However, this does not necessarily mean that the crystallographic *a*, *b*, and *c* axes are aligned three-dimensionally because the *a* and *c* axes do not coincide with the χ_1, χ_2 axes. Due to the axial nature of magnetic axes, a π rotation of a microcrystal about the magnetic axes gives rise to an additional crystal orientation that has an equal magnetic energy. If a unit cell containing molecules A_1(*lmn*) and A_2(*-l-mn*) is rotated by π about the χ_1 axis, two molecules A_3(*l-m-n*) and A_4(*-lm-n*) are created [**Fig. 2**]. These four molecules having mutually different orientations are described by the point group (222).[4] This symmetry is a characteristic of MOMA prepared from monoclinic crystals with the point group 2. Owing to this (222) symmetry, a cellobiose MOMA can be equivalent to the orthorhombic crystal with point group (222), whereby the χ-frame corresponds to the crystallographic *abc* frame of the orthorhombic system.

3.3.2.3 Procedure to determine the principal values and principal axes

The chemical shift tensors $\boldsymbol{\sigma}^{\chi}$s relative to the χ-frame, which are symmetric, are defined as

$$\boldsymbol{\sigma}^{\chi} = \begin{pmatrix} \sigma_{11} & \sigma_{12} & \sigma_{13} \\ \sigma_{12} & \sigma_{22} & \sigma_{23} \\ \sigma_{13} & \sigma_{23} & \sigma_{33} \end{pmatrix}, \begin{pmatrix} \sigma_{11} & \sigma_{12} & -\sigma_{13} \\ \sigma_{12} & \sigma_{22} & -\sigma_{23} \\ -\sigma_{13} & -\sigma_{23} & \sigma_{33} \end{pmatrix}, \begin{pmatrix} \sigma_{11} & -\sigma_{12} & -\sigma_{13} \\ -\sigma_{12} & \sigma_{22} & \sigma_{23} \\ -\sigma_{13} & \sigma_{23} & \sigma_{33} \end{pmatrix}, \begin{pmatrix} \sigma_{11} & -\sigma_{12} & \sigma_{13} \\ -\sigma_{12} & \sigma_{22} & -\sigma_{23} \\ \sigma_{13} & -\sigma_{23} & \sigma_{33} \end{pmatrix}$$

(1)

for the molecules A_1(*lmn*), A_2(*-l-mn*), A_3(*l-m-n*), and A_4(*-lm-n*), respectively. The tensors $\boldsymbol{\sigma}^{\chi}$ is transformed into the expression relative to the principal $\sigma_1\sigma_2\sigma_3$ frame

(σ-frame) as

$$\boldsymbol{\sigma} = \mathbf{R}_\sigma \boldsymbol{\sigma}^\chi \mathbf{R}_\sigma^{-1}, \qquad (2)$$

where $\mathbf{R}_\sigma$ is the transformation matrix whose *ij* component is defined as $(\mathbf{R}_\sigma)_{ij} = \mathbf{s}_i \cdot \mathbf{k}_j$ with $\mathbf{s}_i$ and $\mathbf{k}_j$ being the normalized orthogonal base vectors for the σ- and χ-frames, respectively [**Fig. 3a**]. The tensor $\boldsymbol{\sigma}$ is diagonal whose components are σ_1, σ_2, and σ_3. The principal values and principal axes of the tensor $\boldsymbol{\sigma}$ are determined as the eigenvalues and eigenvectors of the tensor $\boldsymbol{\sigma}^\chi$, respectively.

The tensor $\boldsymbol{\sigma}^\chi$ is transformed into

$$\boldsymbol{\sigma}^{\mathrm{L}} = \mathbf{R}_{\mathrm{L}} \boldsymbol{\sigma}^\chi \mathbf{R}_{\mathrm{L}}^{-1}, \qquad (3)$$

expressed with respect to the laboratory *xyz* frame (L-frame), where $\mathbf{R}_{\mathrm{L}}$ is the transformation matrix whose *ij* component is defined by $(\mathbf{R}_{\mathrm{L}})_{ij} = \mathbf{e}_i \cdot \mathbf{k}_j$ with $\mathbf{e}_i$ being the normalized orthogonal base vectors for the L-frame [**Fig. 3b**].

We use three experimental settings (i), (ii), and (iii) shown in **Fig. 4**. In these settings, MOMA samples, M1, M2, and M3, are set such that (i) $\chi_3 \perp \mathbf{B}_0$, (ii) $\chi_1 \perp \mathbf{B}_0$, and (iii) $\chi_2 \perp \mathbf{B}_0$, where $\mathbf{B}_0$ is the NMR magnetic field. In each setting, the sample is rotated by an angle Ω about the respective axes. When $\Omega = 0$, three settings correspond to (i-0) $\chi_1 \parallel \mathbf{B}_0$, $\chi_3 \perp \mathbf{B}_0$, (ii-0) $\chi_2 \parallel \mathbf{B}_0$, $\chi_1 \perp \mathbf{B}_0$, and (iii-0) $\chi_3 \parallel \mathbf{B}_0$, $\chi_2 \perp \mathbf{B}_0$.

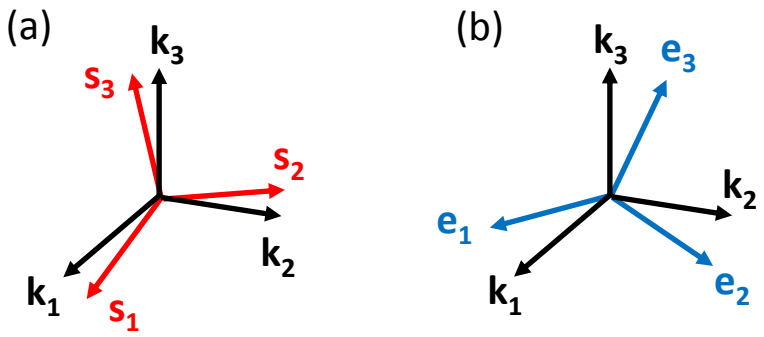

Fig. 3 Relationship of the magnetic frame (χ-frame) with (a) the principal frame (σ-frame) and (b) the laboratory frame (L-frame). Orthogonal unit base vectors in each frame are represented by $\mathbf{s}_i$ (σ-frame), $\mathbf{k}_i$ (χ-frame), and $\mathbf{e}_i$ (L-frame), respectively, where i=1,2,3.

The rotation matrices $\mathbf{R}_{\mathrm{L}}$ for the settings (i), (ii), and (iii) are expressed as follows:

$$\mathbf{R}_{\mathrm{L}}^{(\mathrm{i})}=\begin{pmatrix}0 & 0 & 1\\ \sin\Omega & -\cos\Omega & 0\\ \cos\Omega & \sin\Omega & 0\end{pmatrix},\quad \mathbf{R}_{\mathrm{L}}^{(\mathrm{ii})}=\begin{pmatrix}1 & 0 & 0\\ 0 & \sin\Omega & -\cos\Omega\\ 0 & \cos\Omega & \sin\Omega\end{pmatrix},\quad \mathbf{R}_{\mathrm{L}}^{(\mathrm{iii})}=\begin{pmatrix}0 & 1 & 0\\ -\cos\Omega & 0 & \sin\Omega\\ \sin\Omega & 0 & \cos\Omega\end{pmatrix}. \tag{2}$$

The experimentally observed chemical shift is related to the components of $\boldsymbol{\sigma}^{\chi}$ through the relationship $\sigma_{zz}^{\mathrm{L}}=(\mathbf{R}_{\mathrm{L}}\boldsymbol{\sigma}^{\chi}\mathbf{R}_{\mathrm{L}}^{-1})_{33}$. With the setting (i) at $\Omega=0$, referred to as (i-0), the observed values of σ_{zz}^{L}s for four different molecules A_1, A_2, A_3, and A_4 are the same: (i-0) $\sigma_{zz}^{\mathrm{L}}=\sigma_{11}^{\chi}$. Similarly, (ii-0) $\sigma_{zz}^{\mathrm{L}}=\sigma_{22}^{\chi}$ and (iii-0) $\sigma_{zz}^{\mathrm{L}}=\sigma_{33}^{\chi}$. With the settings (i), (ii), and (iii) at Ω=45°, referred to as (i-45), (ii-45), and (iii-45), we observe two peaks for each of these settings: (i-45) $\sigma_{zz}^{\mathrm{L}}=(\sigma_{11}^{\chi}+\sigma_{22}^{\chi}\pm 2\sigma_{12}^{\chi})/2$, (ii-45) $\sigma_{zz}^{\mathrm{L}}=(\sigma_{22}^{\chi}+\sigma_{33}^{\chi}\pm 2\sigma_{23}^{\chi})/2$,

and (iii-45) $\sigma_{zz}^{\mathrm{L}} = (\sigma_{11}^{\chi} + \sigma_{33}^{\chi} \pm 2\sigma_{13}^{\chi})/2$, giving rise to six equations. Then, the total of nine equations are derived from the above experiments and they are used to determine six unknown values, σ_{11}^{χ}, σ_{22}^{χ}, σ_{33}^{χ}, σ_{12}^{χ}, σ_{23}^{χ}, and σ_{13}^{χ}. There is an arbitrariness of the sign of σ_{12}^{χ}, σ_{23}^{χ}, and σ_{13}^{χ}. Determination of these six values is performed by the least square method. Now, the principal values σ_1, σ_2, and σ_3, and the principal axes $\mathbf{s}_1$, $\mathbf{s}_2$, and $\mathbf{s}_3$ of the tensor $\boldsymbol{\sigma}$ are derived as the eigenvalues and eigenvectors of the tensor $\boldsymbol{\sigma}^{\chi}$.

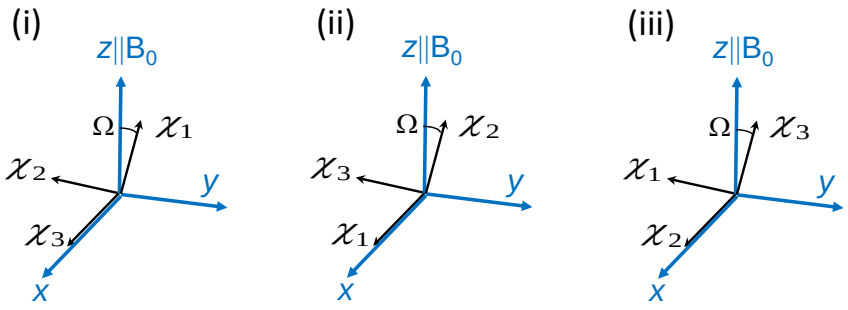

Fig. 4 Experimental settings of MOMA samples in a probe. The NMR magnetic field $\mathbf{B}_0$ is in the *z* direction and the sample rotation axis is laboratory *x* axis. Setting (i): sample M1 is set with $\chi_3 \| x$ axis; settings are referred to as (i-0) and (i-45) when Ω=0 and 45°, respectively. Setting (ii): sample M2 is set with $\chi_1 \| x$ axis; settings are referred to as (ii-0) and (ii-45) when Ω=0 and 45°, respectively. Setting (iii): sample M3 is set with $\chi_2 \| x$ axis; settings are referred to as (iii-0) and (iii-45) when Ω=0 and 45°, respectively. It is noted that $\chi_1 \| \mathbf{k}_1$, $\chi_2 \| \mathbf{k}_2$, and $\chi_3 \| \mathbf{k}_3$, where vector **k**s are defined in Fig. 3.

3.3.3 Simulation for peak assignment

The chemical shift values of C1 carbon determined by SUPER range as σ_1=119.4, σ_2=102.9, and σ_3=89.7 ppm and those of C1' range as σ_1'=122.1, σ_2'=99.4, and σ_3' =70.7 ppm [**Fig. 5**]. Because of these large anisotropies in chemical shifts, C1 and C1′ carbons exhibit severe overlapping in the spectra obtained under experimental settings (i), (ii), and (iii). This causes difficulties in assigning the peaks under consideration. In addition, peaks from other carbons may interfere with the assignment.

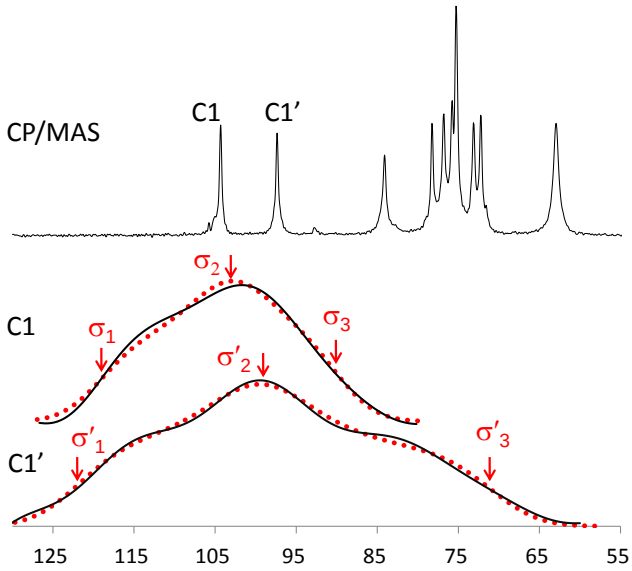

Fig. 5 CP/MAS spectrum and powder patters of C1 and C1′ carbons obtained by SUPER of cellobiose. Dotted red curves in powder spectra are results by simulation and principal values obtained by the simulation are indicated by arrows.

In order to assign C1 and C1′ carbons, we first perform simulations to find approximate locations of the peaks. The simulation is based on the local symmetry assumption. The ^{13}C chemical shift tensor is strongly related to the anisotropy in electron density around the resonance nucleus. The shielding is stronger in the

direction where the electron density is higher. The hybridization of the carbon and the atoms bonding to it dominates the electron environment. So the anisotropy of the chemical shift tensor of a ^{13}C nucleus depends on the bonding symmetry of the nuclei.[2]

The C1 and C1′ carbons are bonding to two oxygen atoms [**Fig. 6**]. The C-O bond is dominant direction of chemical shielding because the electron density is high in this direction. The bond length C1-O1 is shorter than that of C1-O5 bond by 0.031Å, and hence the most shielded direction is close to C1-O1 direction and the least shielded direction is close to the direction perpendicular to the O1-C1-O5 plane. The C1′-O1′ bond is shorter than the C1′-O5′ bond by 0.057 Å, and hence the most shielded direction is close to C1′-O1′ direction and the least shielded direction is close to the direction perpendicular to the O1′-C1′-O5′ plane. These assumptions are employed and confirmed experimentally for several saccharides.[1, 2] Therefore, we assume in the simulation that the σ_3 axis is parallel to the C1-O1 bond and the σ_1 axis is perpendicular to the O1-C1-O5 plane; σ_3' axis is parallel to the C1′-O1′ bond and the σ_1' axis is perpendicular to the O1′-C1′-O5′ plane. Experimental values of σ_1, σ_2, and σ_3 for C1 and σ_1', σ_2', and σ_3' for C1' determined by SUPER were used in simulation. Table 1 summarizes the results of the simulation.

3.3.4 Peak assignment and determination of the tensor $\boldsymbol{\sigma}^{\chi}$

The spectra obtained under the settings (i), (ii), and (iii) for $\Omega = 0$ and $\Omega = 45^{\circ}$ are shown in **Fig. 7**. In this figure, the locations of the peaks for the C1 and C1′ carbons predicted by simulation are indicated by thin arrows. The actual locations of the peaks are found in the vicinity of these predicted locations and indicated by thick arrows. The

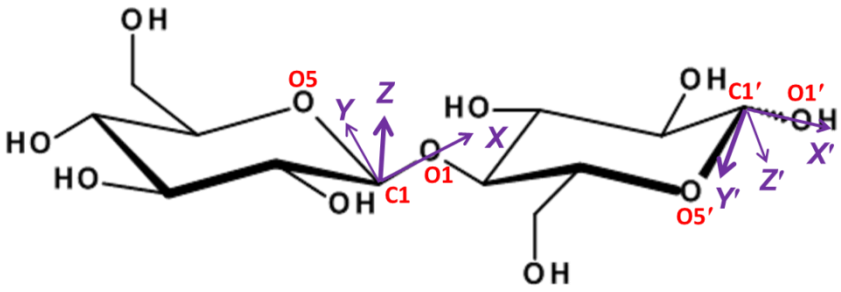

Fig. 6 Molecular axes (*XYZ*) at C1 and (*X′Y′Z′*) at C1′ carbons. The *X* axis is parallel to the C1-O1 bond, the *Y* axis is on the O1-C1-O5 plane, and the *Z* axis is defined following the right-handed rule. The *X′* axis is parallel to the C1′-O1′ bond, the *Y′* axis is on the O1′-C1′-O5′ plane, and the *Z′* axis is defined following the right-handed rule. In simulations, it is assumed that $X \| \sigma_3$, $Y \| \sigma_2$, $Z \| \sigma_1$, $X' \| \sigma_3'$, $Y' \| \sigma_2'$, and $Z' \| \sigma_1'$.

C1	(i-0)	105.6	(i-45)	108.3 93.8
	(ii-0)	96.6	(ii-45)	105 101.5
	(iii-0)	109.8	(iii-45)	118.7 96.7
C1′	(i-0)	104.9	(i-45)	117.2 95.7
	(ii-0)	108.1	(ii-45)	110.8 76.5
	(iii-0)	79.2	(iii-45)	91.5 92.7

Table 1 Simulation results for peak positions (ppm) expected to appear under different experimental settings, (i-0), (ii-0), (iii-0), (i-45), (ii-45), and (iii-45) for C1 and C1′ carbons.

results of the assignment are summarized in Table 2. Applying the least square method to the values tabulated in Table 2, we obtain the tensors $\boldsymbol{\sigma}^{\chi}$(C1) for C1 carbons as follows:

$$\boldsymbol{\sigma}^{\chi}(\text{C1}) = \begin{pmatrix} 109.4 & -7.7 & 8.0 \\ -7.7 & 98.1 & -3.1 \\ 8.0 & -3.1 & 106.6 \end{pmatrix}, \qquad \text{(5a)}$$

$$\begin{pmatrix} 109.4 & 7.7 & -8.0 \\ 7.7 & 98.1 & 3.1 \\ -8.0 & 3.1 & 106.6 \end{pmatrix} \qquad \text{(5b)}$$

The tensors for the other three molecules can be generated according to eq. (1). Either one of eq. (5) is correct.[11] The principal values derived are $\sigma_1 = 119.1$, $\sigma_2 = 100.9$, $\sigma_3 = 94.1$ ppm from eq.(5a) and $\sigma_1 = 117.1$, $\sigma_2 = 105.7$, $\sigma_3 = 91.3$ ppm from eq.(5b). These should be compared to $\sigma_1 = 119.4$, $\sigma_2 = 102.9$, $\sigma_3 = 89.7$ ppm determined by SUPER. It is difficult to tell which is close to those by SUPER. In **Fig. 8(a)**, the principal σ_1, σ_2, and σ_3 axes of C1 carbon are shown. The blue and red arrows are those determined using eqs (5a) and (5b), respectively. According to the criteria [1, 11], we conclude that eq (b) provides a better result because the σ_3 axis (red) derived from (5b) is closer to the C1-O1 bond. In Table 3, the principal values and direction cosines in molecular *XYZ* frame [**Fig. 6**] are summarized.

On the other hand, we obtain the tensors $\boldsymbol{\sigma}^{\chi}$(C1′) for C1′ carbons uniquely as follows because σ_{13}^{χ} component happens to vanish:

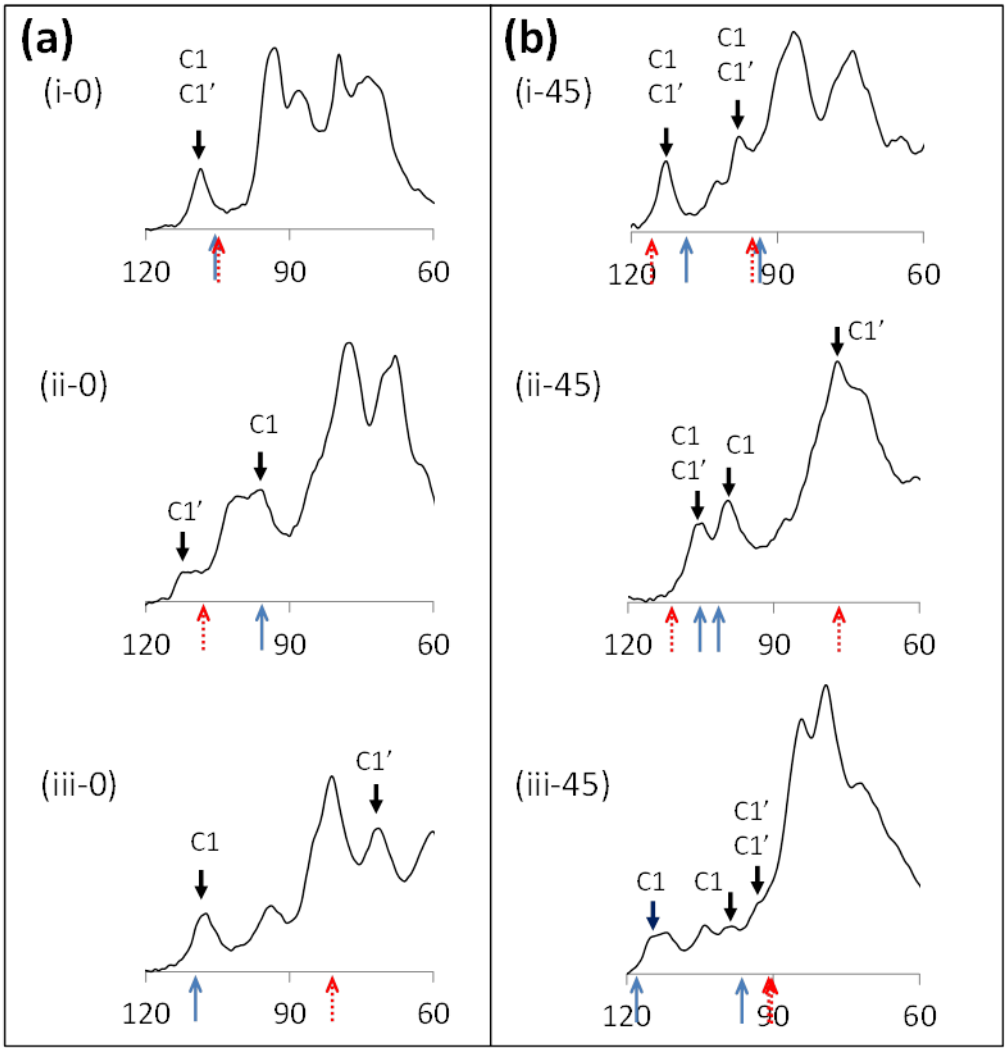

Fig. 7　Spectra observed under (a) settings (i-0), (ii-0), and (iii-0) and (b) settings (i-45), (ii-45), and (iii-45).　Peak positions (ppm) for C1 and C1′ predicted by simulation (Table 1) are indicated by thin arrows (blue for C1 and dotted red for C1′) and those assigned are indicated by thick arrows.

C1	(i-0)	108.7	(i-45)	113.2 97.8
	(ii-0)	96.3	(ii-45)	105.4 99.3
	(iii-0)	107.6	(iii-45)	115.0 99.0
C1′	(i-0)	108.7	(i-45)	113.2 97.8
	(ii-0)	112.0	(ii-45)	105.4 77.0
	(iii-0)	71.5	(iii-45)	93.0 93.0

Table 2 Peak positions (ppm) determined from the spectra displayed in Fig. 7, with the help of simulation peak positions (Table 1) indicated in Fig. 7.

Carbons nucleus	Principal value of tensor	Direction cosines with respect to		
		X (*X*′)	*Y* (*Y*′)	*Z* (*Z*′)
C1	σ3 91.3	0.9949	-0.0509	-0.0870
	σ2 105.8	0.0292	0.9718	-0.2340
	σ1 117.1	0.0964	0.2303	0.9683
C1′	σ3′ 68.4	0.9917	-0.1090	0.0685
	σ2′ 103.3	0.1132	0.9917	-0.0604
	σ1′ 118.9	-0.0613	0.0677	0.9958

Table 3 Principal values and direction cosines of the C1 and C1′ chemical shift tensors relative to the molecular frame defined in Fig. 6.

$$\boldsymbol{\sigma}^{\chi}(\mathrm{C1}') = \begin{pmatrix} 108.0 & -7.7 & 0.0 \\ -7.7 & 109.0 & 14.2 \\ 0.0 & 14.2 & 73.6 \end{pmatrix}. \qquad (6)$$

The principal values are calculated as $\sigma_1 = 118.9$, $\sigma_2 = 103.2$, $\sigma_3 = 68.5$ ppm, which are compared to σ_1' =122.1, σ_2' =99.4, and σ_3' =70.7 ppm obtained by SUPER. The principal σ_1', σ_2', and σ_3' axes are shown in **Fig. 8(b)**. In Table 3, the principal values and direction cosines in molecular *X′Y′Z ′*frame [**Fig. 6**] are summarized.

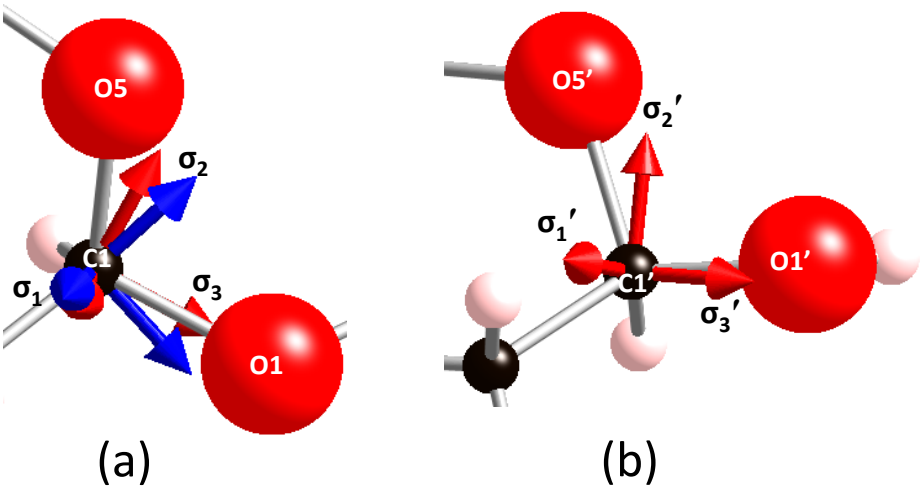

Fig. 8 (a) Principal axes of C1 carbon determined from eqs (5a, b). Blue and red arrows correspond to eqs (5a) and (5b), respectively. (b) Principal axes of C1′ determined from eq (6).

4. Conclusions

The chemical shift tensors of C1 and C1′ carbons of cellobiose crystals were

determined from its microcrystalline powder sample by using MOMA samples. In this study, MOMA samples were rotated about its magnetic axes, while a single crystal is rotated about its crystallographic axes in conventional single crystal NMR methods. Since a MOMA is formed in a rod-like shape and its magnetic axis coincides with the rod axis, the rotation axis is easily identified when performing the sample rotating measurements. This is a marked contrast to the rotation of single crystals. We conducted six measurements at designated sample orientations with respect to the applied field to determine six components of the chemical shift tensor expressed relative to χ-frame. We obtained two chemical shift tensors for C1 carbon, between which the correct one was selected by the criteria that σ_3 direction is close to the C1-O1 bond vector. We have demonstrated that the use of MOMAs is of great advantage when large single crystals are unavailable, whereby the rotations about the magnetic axes are appropriate choices.

References

[1] Sastry, D. L.; Takegoshi, K.; McDowell, C. A., *Carbohydrate Research* **1987**, *165* (2), 161-171.

[2] Sherwood, M. H.; Alderman, D. W.; Grant, D. M., *Journal of Magnetic Resonance Series A* **1993**, *104* (2), 132-145.

[3] Kimura, T.; Yoshino, M., *Langmuir* **2005**, *21* (11), 4805-4808; Kimura, T.; Kimura, F.; Yoshino, M., *Langmuir* **2006**, *22* (8), 3464-3466; Kimura, T.; Chang, C.; Kimura, F.; Maeyama, M., *Journal of Applied Crystallography* **2009**, *42*, 535-537; Kimura, F.; Kimura, T.; Matsumoto, K.; Metoki, N., *Crystal Growth & Design* **2010**, *10* (1), 48-51; Kimura, F.; Kimura, T.; Oshima, W.; Maeyama, M.; Aburaya, K., *Journal of Applied Crystallography* **2010**, *43*, 151-153.

[4] Kimura, F.; Mizutani, K.; Mikami, B.; Kimurat, T., *Crystal Growth & Design* **2011**, *11* (1), 12-15.

[5] Kimura, F.; Oshima, W.; Matsumoto, H.; Uekusa, H.; Aburaya, K.; Maeyama, M.; Kimura, T., *Crystengcomm* **2014**, *16* (29), 6630-6634.

[6] Liu, S. F.; Mao, J. D.; Schmidt-Rohr, K., *Journal of Magnetic Resonance* **2002**, *155* (1), 15-28.

[7] Kalenius, E.; Kekaelaeinen, T.; Neitola, R.; Beyeh, K.; Rissanen, K.; Vainiotalo, P., *Chemistry-a European Journal* **2008**, *14* (17), 5220-5228.

[8] Nye, J. F., Physical properties of crystals : their representation by tensors and matrices. Clarendon Press: Oxford, 1985.

[9] Song, G.; Kimura, F.; Kimura, T.; Piao, G., *Macromolecules* **2013**, *46* (22), 8957-8963.

[10] Guangjie, S.; Matsumoto, K.; Fujita, K.; Kimura, F.; Kimura, T., *Japanese Journal of*

Applied Physics **2012**, *51* (6).

[11] Shekar, S. C.; Ramamoorthy, A.; Wittebort, R. J., *Journal of Magnetic Resonance* **2002**, *155* (2), 257-262.

Chapter4

Orientational distribution of cellulose nanocrystals in cellulose whiskers (Cotton, Ramie and Wood) as studied by diamagnetic anisotropy

4.1 Introduction

Cellulose whiskers (CWs), especially those of nanometer size, have drawn increasing attention because of their renewable nature and excellent physical and chemical properties.[1–4] Depending on the source of celluloses and hydrolysis conditions, the whiskers can be obtained in a variety of sizes, shapes, and degrees of crystallinity,[5,6] which could affect the performance of the final products such as composite materials. After biosynthesis, cellulose chains crystallize in nanocrystals (CNCs) that further form hierarchical suprastructures until ending up in macrofibers.[2,7,8] The elucidation of these suprastructures existing in CWs is important not only for an understanding of their formation mechanism but also for their proper characterization. There are several aspects of these suprastructures, among which the orientational distribution of the CNCs is of great interest because the orientation is one of the dominant factors affecting the physical properties of CWs such as mechanical, optical, dielectric, and thermal properties.

X-ray diffraction analysis is commonly used for the determination of crystal structures and the characterization of crystal orientations. If macrofibers are under consideration, the fiber X-ray pattern is easily acquired and the orientational distribution, such as the microfibril angle (MFA) with respect to the axis of the macrofiber, is reflected in a broadening of diffraction spots along the azimuthal direction.[9] However, in the case of whickers, only powder patterns are available, which hinders a corresponding orientational analysis. We need to align individual whisker particles to obtain a fiber

pattern. There are several ways to align CWs, including magnetic,[10–18] electric,[19,20] and mechanical[21] methods. Among these, the application of a magnetic field is a versatile technique.[22] By using static and rotating magnetic fields, we can obtain two types of uniaxial alignments (a uniaxial alignment of the easy and of the hard magnetization axes) and, accordingly, two fiber patterns, thereby enhancing the information needed for the structure analysis.

In this study, we firstly investigate the orientational distribution of CNCs in a Cotton CW using two X-ray fiber patterns from CWs aligned under static or rotating magnetic field, respectively. The orientational disorder of CNCs is related to the correlation length of the anisotropy of the magnetic susceptibility. Then, this method was applied to Ramie and Wood CW to study orientational distribution of nanocrystals to determine the correlation lengths.

4.2 Experiment

4.2.1 Cotton

4.2.1.1 Preparation of cotton cellulose microwhiskers

Cotton cellulose powder (Whatman CF11, 11 g) was hydrolyzed with hydrochloric acid (5 mol/L, 310 ml) at 80 °C for 325 min. The suspension was then diluted to stop the reaction, followed by centrifugation. The isolated cellulose was washed once with water and centrifuged again. The precipitate was dialyzed against water in a VISKING dialysis membrane (Nihon Medical Science, Inc.) for a few days until the water pH value became constant.

The suspension thus obtained was diluted by excess water. Cellulose particles that sank after 1.5 h were collected and marked as fraction 2 (F2). The supernatant

was allowed to stand for a few days and the precipitate was collected and marked as fraction 1 (F1). In addition, the original CF11 sample was passed through a 20 μm mesh, and the powder that passed through was collected and marked as fraction 3 (F3).

The size distribution of the CWs of each fraction was determined by observation with a microscope. Each fraction was dispersed in an ultraviolet (UV)-curable monomer (Kyoritsu Chemical XVL-90K) to prepare 10-wt% suspensions that were subjected to a magnetic field, followed by photopolymerization of the monomer to consolidate the alignment.

4.2.1.2 Preparation of magnetically oriented whiskers

The UV-curable monomer suspension F1 was divided into two parts and each of them was poured into a plastic container (5 mm diameter; 8 mm height). One suspension was exposed to a horizontal static magnetic field of 8 T (a Sumitomo Heavy Industry cryocooler-cooled superconducting magnet) for 40 min and then irradiated by UV light for 1 h, with the constant magnetic field being kept applied, to photopolymerize the monomer and, thereby, to consolidate the alignment. This sample is referred to as M1S ("S" stands for static). The other sample was rotated in the same horizontal static magnetic field at 35 rpm for 1 h with the rotation axis set vertically (perpendicular to the magnetic field). Then, the suspension was UV-irradiated for 1 h with the magnetic field and the rotation being kept applied, to photopolymerize the monomer. This sample is referred to as M1R ("R" stands for rotating). The same procedure was applied to F2 and F3 to prepare magnetically oriented samples, which are referred to as M2S, M2R, M3S, and M3R.

4.2.1.3 X-ray diffraction measurement

Wide angle X-ray diffraction measurements were performed using a MAC Science

Dip 2020 diffractometer equipped with an MXP18HF22 rotating anode generator (45 kV, 84 mA). The 2D detector employed was a Mac Science Dip 2020 (20-cm plate, 80-μm pixel, and 2500 x 2500 pixels in number). The transmittance mode was used. The exposure time was 45 min. Graphite-monochromated Cu Kα radiation was used ($\lambda = 1.54078$Å). The collimator size was 0.9 mm in diameter, sample-to-detector distance was 150.0 mm, and divergence of the X-ray beam was 0.5°. The specimen of ca. 1.2-mm thickness was cut from approximately the center of the photopolymerized samples of M1S, M2S, M3S, M1R, M2R, and M3R and subjected to the X-ray measurement.

The background diffraction due to the photopolymerized monomer was removed as follows: The 2D diffraction pattern of the pure photopolymerized monomer was measured, and subtracted from that of whisker-containing sample. Since the thickness was slightly different depending on specimens, the factor of the subtraction was determined so that at the 2θ scan the baseline around the (200) plane becomes flat. After the subtraction was performed, the azimuthal scan for the (200) plane was made.

4.2.2 Ramie

4.2.2.1 Preparation of ramie cellulose microwhiskers

Raw ramie fiber (7.89 g) was cut by a sharp blade and hydrolyzed with hydrochloric acid (6 mol/L, 500 ml) at 76 °C for 330 min. The suspension was then diluted to stop the reaction, followed by centrifugation. The precipitate was dialyzed against water in a dialysis membrane for a few days until the water pH value became constant.

The suspension thus obtained was diluted by excess water. Cellulose particles that sank after 20 min were collected. The collected part was diluted by excess water

again and after 20 min, the precipitation was collected and marked as fraction 3 (F3R). The supernatant was allowed to stand for about 2 h and the precipitate was collected and marked as fraction 2 (F2R). The supernatant was allowed to stand for about 50min and the precipitate was removed. The supernatant was allowed to stand for about 12 days and the precipitate was collected and marked as fraction 1 (F1R).

The size distribution of the Ramie CWs of each fraction was determined by observation with a microscope. Each fraction was dispersed in an ultraviolet (UV)-curable monomer (Kyoritsu Chemical XVL-90K) to prepare 5~10 wt% suspensions that were subjected to a magnetic field, followed by photopolymerization of the monomer to consolidate the alignment.

4.2.2.2 Preparation of magnetically oriented whiskers

The procedure is same as in **4.2.1.2**

4.2.2.3 X-ray diffraction measurement

The synchrotron X-ray diffraction measurement was performed at Spring 8. The background diffraction due to the photopolymerized monomer was removed as follows: The 2D diffraction pattern of the pure photopolymerized monomer was measured, and subtracted from that of whisker-containing sample. After the subtraction was performed, the azimuthal scan for the (200) plane was made.

4.2.3 Wood

4.2.3.1 Preparation of wood cellulose microwhiskers

3.03 g Wood cellulose pulp (NBKP) was cut into small pieces with a cutter and then hydrolyzed with hydrochloric acid (5 mol/L, 200 ml) at 70 ºC for 255 min. The suspension was then diluted to stop the reaction, followed by centrifugation. The precipitate was dialyzed against water in a dialysis membrane for a few days until the

water pH value became constant. The suspension thus obtained was diluted by excess water. Cellulose particles that sank after 10min were collected and marked as fraction 3 (F3W).

Sample preparation for other two fractions of wood 4 g wood cellulose pulp (NBKP) was cut into small pieces with a cutter. 640 g H_2O was added in a triangle biker with 4 g wood cellulose. Then, homogenizer was used to disperse the wood cellulose in water. HCl (320 ml, 36%) was added into the suspension. Now the suspension consists of 4 g wood cellulose and HCl (960 ml, 4 mol/L). Hydrolysis was carried out under 82 ºC for 10 h. The acid was removed by centrifugement. HCl (960 ml, 4 mol/L) was used again to hydrolyze the wood cellulose under 82 ºC for 3 h. Then, the acid was removed by centrifugement of suspension two times.

The acid was removed further by the ion exchange resin. Then, the suspension was diluted by excess water. After 6mins, the precipitation was disregarded. The upper layer was allowed to stand for 1h, and collect the precipitation marked as Fraction 2W (F2W). After 10 h, the precipitation was disregarded. After 48 h, the precipitation was again collected as Fraction 1W (F1W).

The size distribution of the Wood CWs of each fraction was determined by observation with a microscope. Each fraction was dispersed in an ultraviolet (UV)-curable monomer (Kyoritsu Chemical XVL-90K) to prepare 5-wt% suspensions for F3W, and 2.3-wt% suspensions for F2W and F1W that were subjected to a magnetic field, followed by photopolymerization of the monomer to consolidate the alignment.

4.2.3.2 Preparation of magnetically oriented whiskers

In this section, it refers to the case of cotton **4.2.1.2**

4.2.3.3 X-ray diffraction measurement

The synchrotron X-ray diffraction measurement was performed at Spring 8. The base line of azimuthal plots was removed using the ImageJ software.

4.3 Results and discussion

4.3.1 Methodology development using cotton cellulose whisker

4.3.1.1 Microscope observation

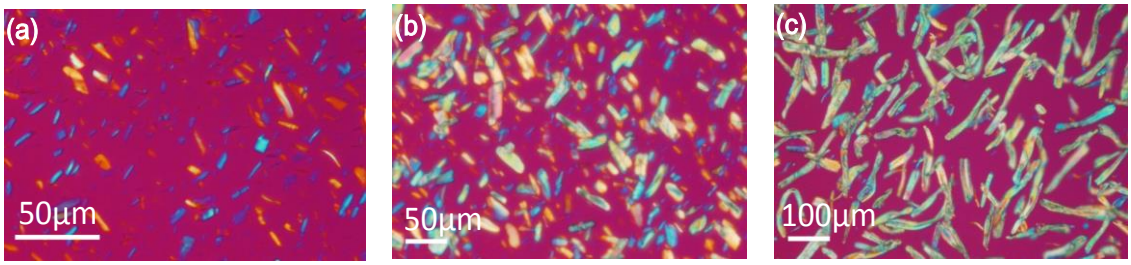

Fig. 1 Cotton cellulose whiskers (CWs) of the three fractions: Suspensions of (a) F1, (b) F2, and (c) F3, observed by polarized optical microscope with a color plate. The average lengths are (a) 8 μm, (b) 23 μm, and (c) 103 μm.

The average size *L* and the aspect ratio *D* of the CWs of the different samples were as follows. Fraction 1 (F1): *L* = 8 μm, *D* = 4.1; fraction 2 (F2): *L* = 23 μm, *D* = 3.2; fraction 3 (F3): *L* = 103 μm, *D* = 6.4. Polarized-optical microscopy (POM) observations of F1, F2, and F3 with a color plate are shown in **Fig. 1**. The optical homogeneity of the whiskers in each fraction is evidently different. The whiskers of sample F3 exhibit multicolors, but those from F1 are almost homogeneous in color. The optically uniform whiskers identified in F1 appear to be fragments derived from larger particles, as observed in F3. Although the whiskers of F1 appear optically uniform, it does not necessary mean that the CNCs are three-dimensionally aligned inside of the CWs used in the present study, because the typical size of CNCs is reported to be 200–350 nm in

length and 5 nm in width for cotton cellulose.[3] If the CNCs are perfectly aligned in the whisker, the CWs should exhibit a biaxial nature; however, as will be discussed later, the CWs of F1 are magnetically uniaxial.

4.3.1.2 Magnetic alignment of CWs

The diamagnetic anisotropy of a biaxial crystal is fully characterized by the magnetic susceptibility tensor that has three different magnetic susceptibility values χ_1, χ_2, and χ_3,[23] where we assume $\chi_1 > \chi_2 > \chi_3$. These values are associated with the magnetic axes; the χ_1- and χ_3-axes are referred to as easy and hard magnetization axes, respectively. In the case of the monoclinic crystal system, the two-fold crystal axis coincides with one of these magnetic axes.[23] The easy magnetization axis aligns in the direction of the applied static magnetic field, whereas the hard magnetization axis aligns in the direction of the *z*-axis when a rotating magnetic field is applied within the *xy*-plane.[24–26] Since the application of a rotating magnetic field to a sample is equivalent to the rotation of the sample in a static magnetic field, these two statements are used interchangeably hereafter.

The native cellulose crystal has two crystal modifications of triclinic I_α[27] and monoclinic I_β.[28] The content of each modification depends on the source of cellulose. Cotton cellulose is rich in I_β modification. The *c*-axis (cellulose chain direction) of the I_β modification is the twofold axis, and hence, it coincides with one of the magnetic axes. Sugiyama et al. reported that the *c*-axis of tunicate cellulose (rich in I_β) coincides with the hard magnetization axis and the *a*-axis (perpendicular to the glucose ring) is close to the easy magnetization axis.[10] Furthermore, it is reported that the chiral nematic phase formed by CNC suspensions aligns with its helical axis parallel to the applied magnetic field, indicating that the *c*-axis is the hard magnetization axis.[11,15]

In a CW, it is assumed that the *c*-axes of the CNCs are approximately aligned in the direction parallel to the whisker axis (long axis) with a certain degree of orientational distribution. Thus, by application of a rotating magnetic field, the whisker axis undergoes uniaxial alignment in the direction parallel to the rotation axis of the magnetic field.

In **Fig. 2**, the geometry of the applied static magnetic field and the sample rotation axis with respect to the laboratory *xyz*-coordinates are shown. **Fig. 3** shows micrographs of the sample M1R. We find that the long axes of individual CWs are aligned parallel to the axis of sample rotation. A uniaxial alignment of the long axes of CWs under a rotating magnetic field is reported previously.[16] Moreover, it is reported that poly(ethylene) short fibers also exhibit a similar alignment behavior.[24]

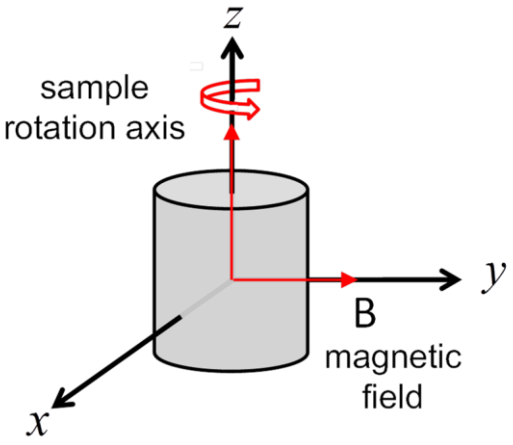

Fig. 2 Schematic of the sample rotation in a static magnetic field. The sample is rotated about the *z*-axis (vertical) and the static magnetic field **B** is applied along the *y*-direction, where *x*, *y*, *z* are the laboratory coordinates.

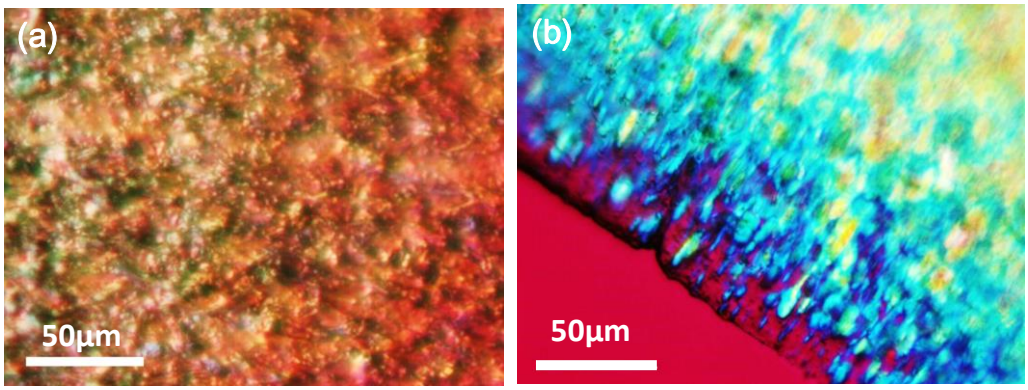

Fig. 3 Micrographs of sample M1R prepared by magnetic alignment of fraction F1 by sample rotation, as shown in Fig. 2. (a) In top view (viewed from the *z*-axis), heads and tails of the CWs are observed. (b) In side view (viewed from the *x*- or *y*-axis), the long axes of the CWs are observed to be uniaxially aligned parallel to the sample rotation axis (*z*-axis).

4.3.1.3 X-ray diffractions of magnetically aligned CWs

Under a rotating magnetic field, the whisker axes (corresponding to the average direction of the *c*-axes of the CNCs) are supposed to align in the direction parallel to the rotation axis and the *a*- and *b*-axes are symmetrically distributed about the *c*-axis. **Fig. 4(a)** shows the X-ray diffraction pattern of M1R, which was prepared under a rotating magnetic field. The diffraction spots are assigned following the crystallographic data of cellulose I_β (*a* = 7.784(8) Å, *b* = 8.201(8) Å, *c* = 10.380(10) Å, γ = 96.5°).[28] In **Fig. 4(a)**, we find that the diffractions from the (200), (110), and $(1\bar{1}0)$ planes are located along the equator that is perpendicular to the direction of the *c*-axis (parallel to the

meridian). The location of the diffractions from the (102) and (012) planes are also reasonably explained.

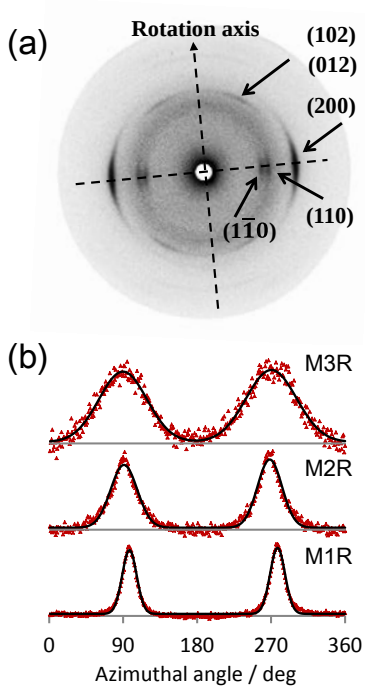

Fig. 4 X-ray results of the samples M1R, M2R, and M3R, prepared by rotation in a magnetic field. The direction of the X-ray is perpendicular to the rotation axis. (a) Diffraction image of sample M1R with the meridian being taken as the direction of the rotation axis (*z*-axis). The meridian corresponds to the CW axes (parallel to the average direction of the *c*-axes of the CNCs constituting a CW). (b) Azimuthal plots of the (200) plane of the samples M1R, M2R, and M3R. The diffraction patterns of M2R and M3R are similar to that of M1R. The line shapes are well fitted by a Gaussian function represented by solid lines, and the half widths increase with the increase in whisker size (M1R < M2R < M3R). The base line of each plot is zero.

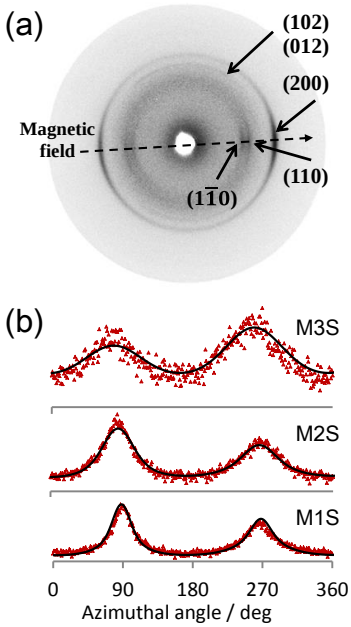

Fig. 5 X-ray results of the samples M1S, M2S, and M3S, prepared under a static magnetic field. The direction of the X-ray is perpendicular to the applied magnetic field. (a) Diffraction image of sample M1S with the equator being taken as the direction of the magnetic field. (b) Azimuthal plots of the (200) plane of the samples M1S, M2S, and M3S. The diffraction patterns of M2S and M3S are similar to that of M1S. The line shapes are well fitted by a simulation based on the orientational distribution model illustrated in Fig. 6. The base lines do not vanish.

Unlike diffractions from a single crystal (CNC), the diffractions in **Fig. 4(a)** are not very sharp but form arcs. There are two possible reasons for this broadening: (i) the magnetic alignment is not sufficient; and (ii) the magnetic alignment is sufficient, but there is a remaining orientational distribution of the CNCs in a CW. A high degree of magnetic alignment is expressed by the condition $\left|(2\mu_0)^{-1}\chi_a B^2 V\right| >> k_B T$,[22] where μ_0 is the magnetic permeability of vacuum; V is the volume of a whisker; B is the applied magnetic field; k_B is the Boltzmann constant; and T is absolute temperature. The anisotropic magnetic susceptibility χ_a is not available in the present case, but if we assume a typical value of common organic materials,[29] this inequality is sufficiently satisfied in the present experiment because the whisker size is sufficiently large (ca. *L* = 8 μm in length and the aspect ratio *D* = 4.1 for sample F1). In fact, we can prove the inequality numerically if we use the following values: $\mu_0 = 4\pi\times10^{-7}$ H/m, $k_B = 1.38\times10^{-23}$ J/K, $B = 8$ T, $T = 300$ K, $\chi_a = -10^{-8}$, $V = \pi L^3/(4D^2) = 2.4\times10^{-17}$ m^3, resulting in 6.1×10^{-18} J >> 4.1×10^{-21} J. Thus, possibility (i) is ruled out; the broadening in the diffraction patterns is not attributed to an insufficient intensity of the applied magnetic field but originates from the orientational distribution of the *c**-axes of the CNCs about the CW axis.

The distribution of the *a**-axes (and, consequently, of the *b**- and *c**-axes) of the individual CNCs in a CW can be regarded as being of Gaussian type because the azimuthal plot of the (200) plane is well fitted by a Gaussian distribution, as shown in **Fig. 4(b)**. In this figure, the azimuthal plots of MR2 and MR3 are also shown. The standard deviation σ_R of the Gaussian distribution increases with the whisker size, indicating that the orientational disorder of the CNCs increases with the size of the CWs.

Fig. 5(a) shows the X-ray diffraction pattern of M1S, which is prepared under a

static magnetic field without sample rotation. Under this condition, the long axes of the whiskers undergo a planar alignment within the *xy*-plane that is normal to the applied static magnetic field. If we assume that the CWs are biaxial, the diffraction intensities of the (110) and $(1\bar{1}0)$ planes should appear off the equator; however, they appear along the equator. In **Fig. 5(b)**, the azimuthal plots of the (200) plane of M1S, M2S, and M3S are shown. The profile of these plots is in marked contrast to that of M1R, M2R, and M3R shown in **Fig. 4(b)**. That is, the peaks are not fitted by a Gaussian distribution and the base line does not vanish. (The asymmetry of the peaks might be attributed to an imperfect sample mounting when the X-ray measurements are performed.) In addition, the half widths are larger in case of the statically aligned samples. Because the efficiency of the magnetic alignment is higher by a factor of $\sqrt{2}$ for a static than for a rotating field, the half width is expected to be narrower for the statically aligned samples. However, the current observation reveals an opposite behavior.

4.3.1.4 Orientation distribution of CNCs in a CW

In order to rationalize these observations for the static samples, we assume the following orientational distribution. Inside of a CW, the crystallographic reciprocal *a**-, *b**-axes of constituent CNCs are symmetrically distributed about their *c**-axis, as shown in **Fig. 6(a)**. If a static magnetic field is applied, the *c**-axes of the CNCs undergo a planar alignment within the plane perpendicular to the applied field, leading to a distribution of the *a**- and *b**-axes, as shown in **Fig. 6(b)** by solid circles. In addition, since the *c**-axes are assumed to be fluctuating about the long axis of a CW, the solid circles in **Fig. 6(b)** should be convoluted with the Gaussian distribution that characterizes the distribution of the rotating samples. In this model, the distribution of the reciprocal lattice vectors $\mathbf{G}(200)$ (|| *a** axis), $\mathbf{G}(110)$, and $\mathbf{G}(1\bar{1}0)$ are all located

on the solid circles of **Fig. 6(b)**, which rationalizes the locations of these diffractions as observed in **Fig. 5(a)**.

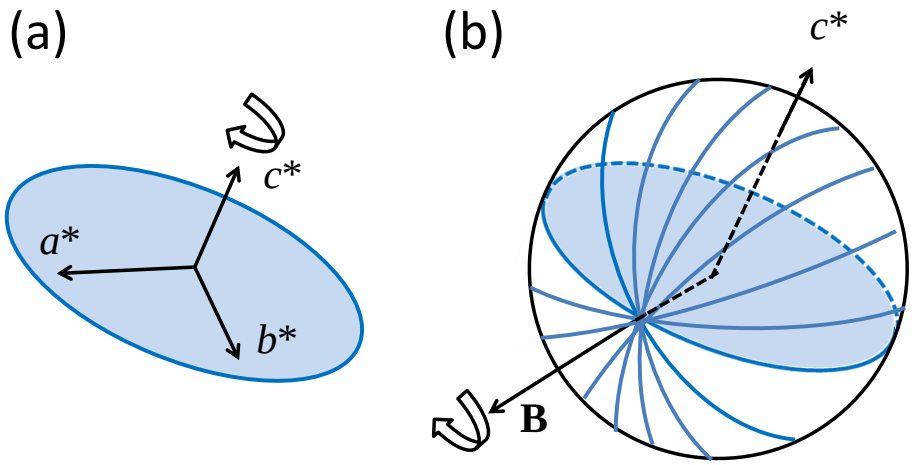

Fig. 6 Model of the distribution of CNCs in a CW. (a) The *c**-axes are uniaxially aligned in the direction of the long axis of a CW with the *a**- and *b**-axes uniformly distributed about the *c**-axes. (b) Under a static magnetic field, the *c**-axes are uniformly distributed about the applied magnetic field **B**. The X-ray beam is impinged from the direction perpendicular to **B**.

The other characteristic feature of the diffraction patterns of the static samples is the line shape of the azimuthal plots, which is shown for the (200) plane in **Fig. 5(b).** The experimentally observed azimuthal plots are well reproduced by the orientational distribution model shown in **Fig. 6(b)**. Simulating the azimuthal plots, the following two factors are considered: (i) the azimuthal profile $f(\beta)$ according to the geometrical distribution of $\mathbf{G}$ for the (200) plane shown in **Fig. 6(b)** is used, with β being the

azimuthal angle, and (ii) the Gaussian distribution $h(\beta)$ determined from the X-ray measurements of the samples aligned in rotating magnetic fields, shown in **Fig. 4(b),** is convoluted with $f(\beta)$ in order to account for the line broadening of $f(\beta)$. Then, the azimuthal plot is finally expressed by

$$F(\beta) = \int_{-\infty}^{\infty} f(\beta_0) h(\beta - \beta_0) d\beta_0 \ . \qquad (1)$$

Details about Eq. (1) are described in Appendix A. The experimentally observed azimuthal plots are shown in **Fig. 5(b)** are well reproduced by $F(\beta)$, demonstrating that the distribution model is appropriate.

4.3.1.5 Orientational correlation

It is clear from **Fig. 4(b)** that the standard deviation σ_{R} of the (200) diffraction peak obtained for the rotating samples increases with the CW size. This indicates that the orientational order of CNCs in a CW is lower if viewed at a larger scale. The decrease in orientational order causes a decrease of the average anisotropic magnetic susceptibility $\langle \chi_{\mathrm{a}} \rangle$ of the CWs. Here, we assume that $\langle \chi_{\mathrm{a}} \rangle$ decays as a function of L as follows:

$$\langle \chi_{\mathrm{a}} \rangle = (\chi_{||} - \chi_{\perp}) \exp\left(-\frac{L}{L_{\mathrm{c}}} \right), \qquad (2)$$

where $\chi_{||} - \chi_{\perp} = \chi_3 - (\chi_1 + \chi_2)/2$ with χ_1 , χ_2 , and χ_3 being the magnetic susceptibilities of the CNCs and L_{c} is the correlation length. It is assumed within the

framework of this model that in the limit of short L ($<< L_c$), the CNCs exist in the form of cellulose nanofibers (CNFs) or their aggregates, in which the *c*-axes of the CNCs are distributed uniaxially. Owing to the crystalline disorder caused by tilting and twisting[7] and/or by the existence of amorphous regions [30] along the fiber axis, a CNF of sufficiently longer scales than the CNCs (typically 100 to 300 nm[3,31]), could be regarded as uniaxial. Likewise, an aggregate of CNFs could also be uniaxial. Therefore, $\chi_{||}$ and $\chi_{\perp}$ are regarded as the magnetic susceptibilities of the CNFs (or its aggregate).

Because we assume a uniaxial nature of the CWs under investigation, the increase in σ_R indicates a decrease in the average anisotropic magnetic susceptibility $\langle \chi_a \rangle$. As shown in Appendix B, $\langle \chi_a \rangle$ is related to the broadening of the X-ray diffraction peaks as follows:

$$\langle \chi_a \rangle = (\chi_{||} - \chi_{\perp}) \exp(-2.6\, \sigma_R^2). \qquad (3)$$

Here, we assume that the azimuthal β plot of the X-ray diffraction is approximated by a Gaussian function with the standard deviation σ_R [**Fig. 4(b)**]. If we combine Eqs. (2) and (3), we obtain a relation between the size L of the CWs and the standard deviation σ_R determined from the X-ray measurements of the rotating samples as follows:

$$\sigma_R^2 = \frac{1}{2.6} \frac{L}{L_c}. \qquad (4)$$

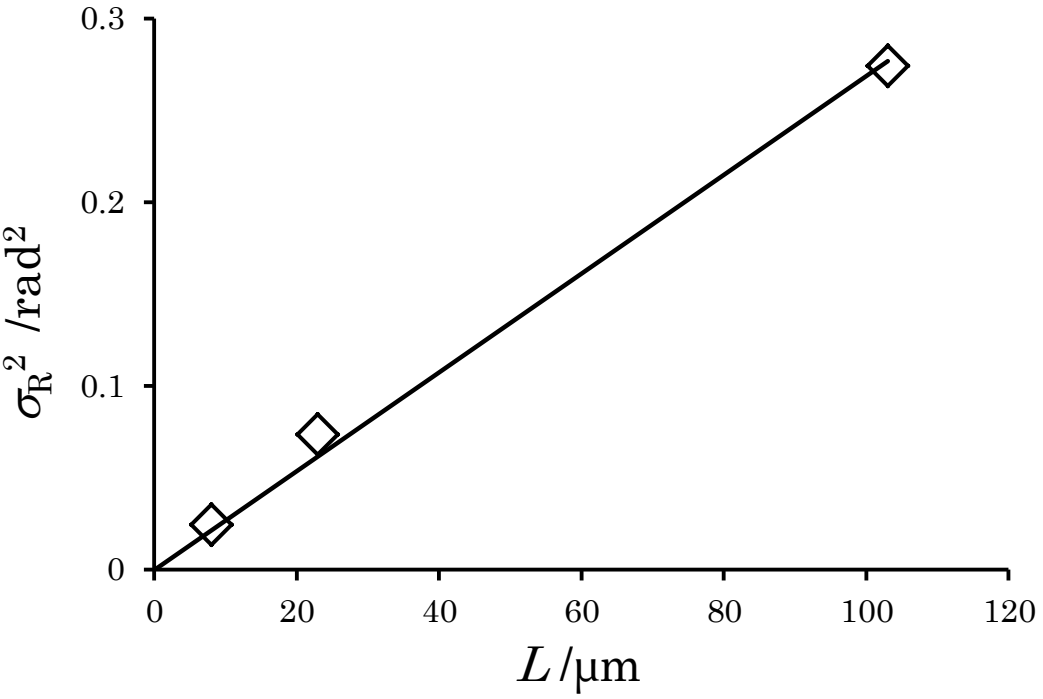

Fig. 7 Plot of the standard deviations σ_R^2 determined from Fig. 4(b) of the rotating samples M1R, M2R, and M3R as a function of the size *L* of the CWs.

In **Fig. 7**, σ_R^2 (rad^2) is plotted against L. The experimental data fall on a straight line passing through the origin, indicating that Eq. (4) is appropriate to describe the experimental observations. From the value of the slope, the correlation length L_c is determined to 142 μm. The value of L_c may depend on the source of the cellulose. The origin of the orientational correlation length is attributed to the orientational distribution of CNFs deposited in the secondary wall of the cell. In a cotton macrofiber, the CNFs are spirally arranged in the secondary wall at a certain MFA [32] that may be different from layer to layer within the secondary wall. If a macrofiber is hydrolyzed into

smaller segments, such as CWs, the spiral nature might become less dominant and a parallel arrangement of the CNFs at a local scale could show up. There may be suprastructures other than the commonly observed spiral arrangement, but in general, it is expected that the orientational disorder of the CNCs within a suprastructure is larger if viewed at a larger scale. Therefore, the disorder decreases upon downsizing. A decrease of the order is evident in the optical micrographs [**Fig. 1]**. The CWs with average size of 8 μm (F1) exhibit a homogeneous color throughout the entire particle, indicating that the orientation of the axes of the CNFs is uniform within a CW. The uniformity in orientation decreases with increasing average size of the CWs (F2 and F3). The correlation length determined above appears to be in good agreement with these microscope observations.

In the present model, a uniaxial segment of CNF or its aggregate is regarded as the smallest unit of the cellulose suprastructure. However, this is not the actual case. If the whisker size is diminished, for example by enhanced hydrolysis, some size will be reached at which the biaxial nature of the CNCs starts to appear, which may be confirmed by the X-ray diffraction patterns of the statically aligned samples. This will certainly occur at sizes of the CNCs as summarized in the literature,[2,3] but it may likewise occur at much larger sizes, depending on the degree of disorder in the CNFs or its aggregate.

4.3.2 Correlation lengths of ramie and wood

4.3.2.1 Ramie cellulose whisker

A theory about correlation length of cellulose nanocrystals has been developed using cotton whiskers. By the same procedures, correlation length of ramie cellulose

whiskers was studied. **Fig.8** shows three fractions of ramie cellulose whiskers (F1R, F2R, and F3R, here R refers to Ramie). **Fig. 9** is the micrograph of the sample prepared by magnetic alignment of Fraction F1R by sample rotation and the alignment can be confirmed directly in **Fig. 9**. **Fig. 10** are the X-ray results of the samples F1R, F2R, and F3R prepared by rotation in a magnetic field. **Fig. 10(a)** is the diffraction image of aligned F1R sample. **Fig. 10(b)** are azimuthal plots of the (200) plane of the three aligned samples, and the line shapes are well fitted by a Gaussian function represented by solid lines. The standard deviation σ_R of the Gaussian distribution can be determined by the fitting process.

The slop of the linear line of ramie cellulose whisker is very small [**Fig. 14**], and it indicates that the correlation length is very large and nanocrystals in the ramie whiskers are aligned with very small orientational disorder. Intercept with y axis is almost zero, and this means that there is no orientational disorder in the cellulose nanocrystals.

4.3.2.2. Wood cellulose whisker

The same procedures were also performed on wood cellulose whiskers to determine the correlation length. **Fig.11** shows three fractions of wood cellulose whiskers (F1W, F2W, and F3W, here W refers to Wood). **Fig. 12** is the micrograph of the sample prepared by magnetic alignment of Fraction F1W by sample rotation and the alignment can be confirmed directly in **Fig. 12**. **Fig. 13** are the X-ray results of the samples F1W, F2W, and F3W prepared by rotation in a magnetic field. **Fig. 13(a)** is the diffraction image of aligned F1W sample. **Fig. 13(b)** are azimuthal plots of the (200) plane of the three aligned samples obtained by ImageJ software, and the line shapes are well fitted by a Gaussian function represented by solid lines. The standard deviation σ_R of the Gaussian distribution can be determined by the fitting process.

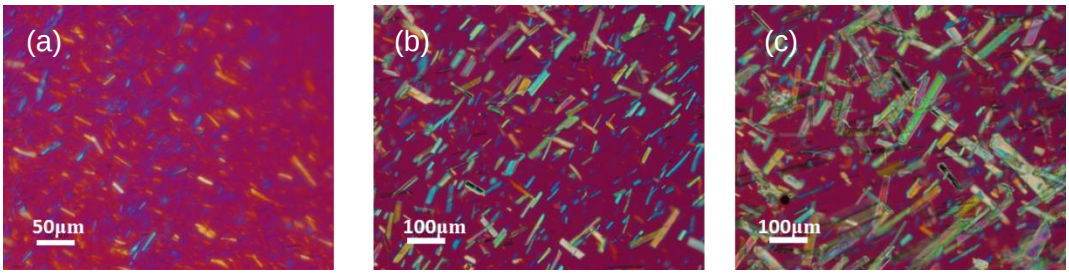

Fig. 8 Ramie whiskers of the three fractions: Suspensions of (a) F1R, (b) F2R, and (c) F3R, observed by polarized optical microscope with a color plate. The average lengths are (a) 17 μm, (b) 44 μm, and (c) 80 μm.

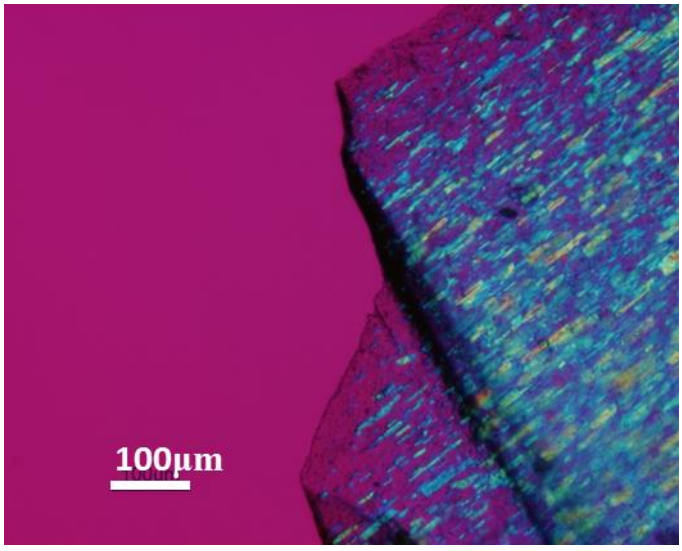

Fig. 9 A micrographs of the sample prepared by magnetic alignment of fraction F1R by sample rotation, as shown in Fig. 2. In side view (viewed from the *x*- or *y*-axis), the long axes of the Ramie CWs are observed to be uniaxially aligned parallel to the sample rotation axis (*z*-axis).

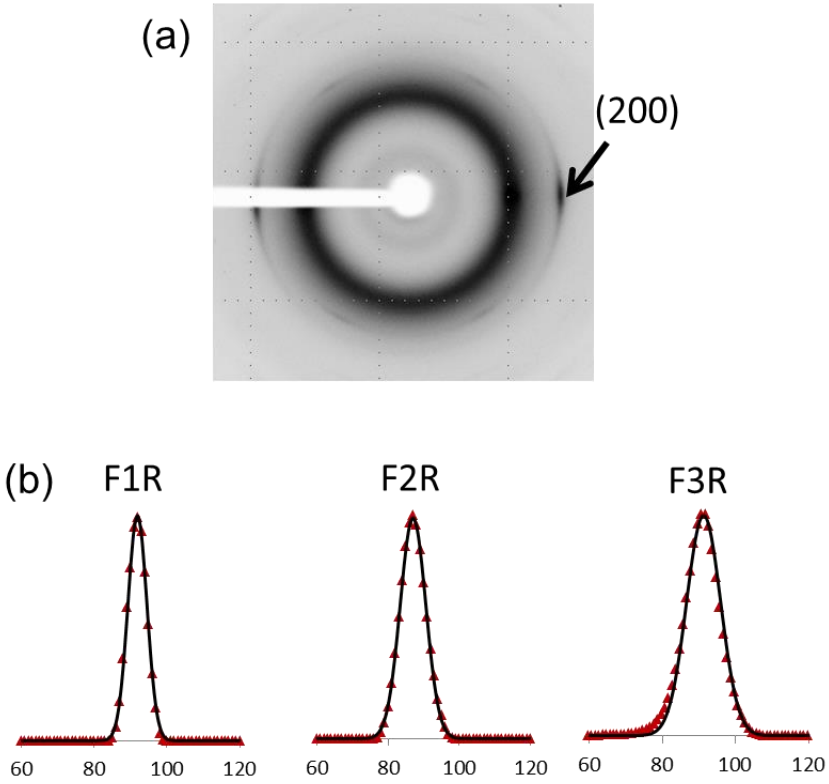

Fig. 10 X-ray results of the samples F1R, F2R, F3R prepared by rotation in a magnetic field. The direction of the X-ray is perpendicular to the rotation axis. (a) Diffraction image of aligned F1R sample, (b) Azimuthal plots of the (200) plane of the three aligned samples. The three diffraction patterns are similar. The line shapes are well fitted by a Gaussian function represented by solid lines. The base line of each plot is zero.

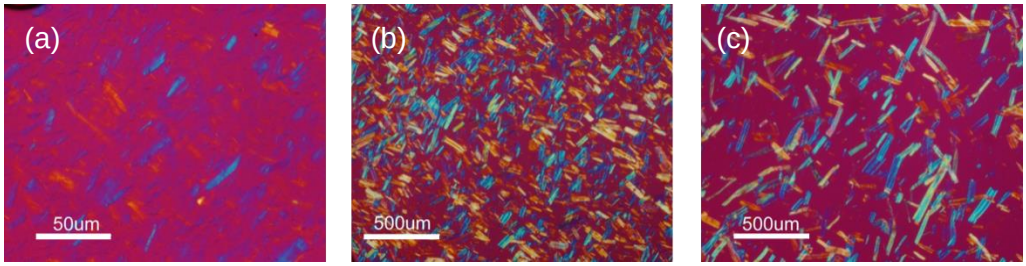

Fig.11 Wood whiskers of the three fractions: Suspensions of (a) F1W, (b) F2W, and (c) F3W, observed by polarized optical microscope with a color plate. The average lengths are (a) 12 μm, (b) 85 μm, and (c) 160 μm.

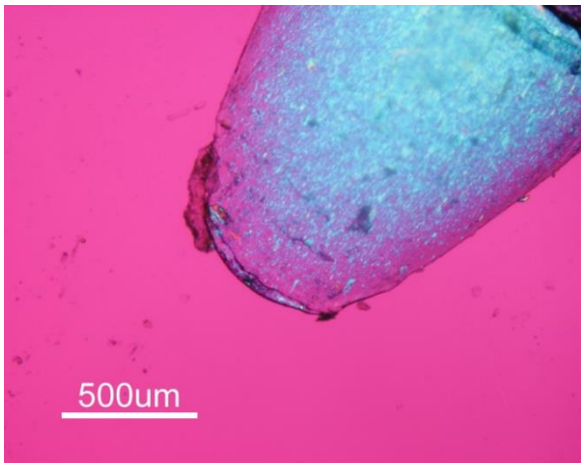

Fig. 12 A micrograph of the sample prepared by magnetic alignment of fraction F1W by sample rotation, as shown in Fig. 2. In side view (viewed from the *x*- or *y*-axis), the long axes of the Wood CWs are observed to be uniaxially aligned parallel to the sample rotation axis (*z*-axis).

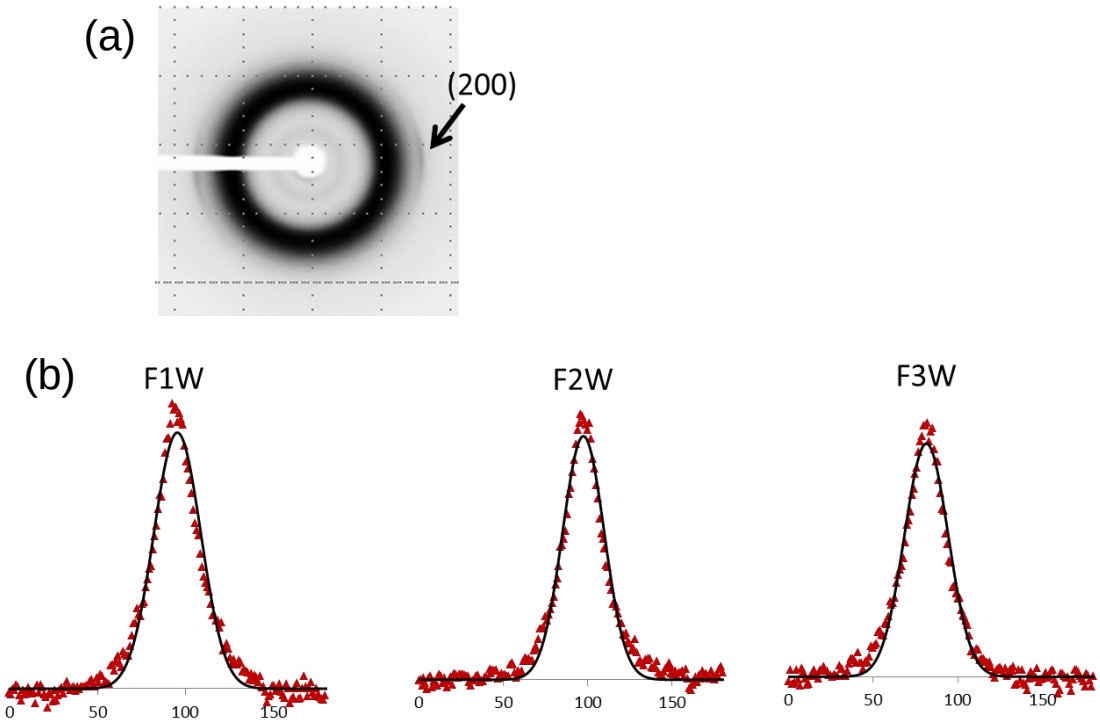

Fig. 13 X-ray results of the samples F1W, F2W, F3W prepared by rotation in a magnetic field. The direction of the X-ray is perpendicular to the rotation axis. (a) Diffraction image of aligned F1W sample, (b) Azimuthal plots of the (200) plane of the three aligned samples. The three diffraction patterns are similar. The line shapes are well fitted by a Gaussian function represented by solid lines. The base line of each plot is zero.

The slop of the linear line of the wood cellulose whisker is also very small (**Fig. 14**), and it indicates that the correlation length is very large and nanocrystals in the wood whiskers are aligned with very small orientational disorder. Intercept with y axis is 0.0524 rad^2 in this study, meaning that there is orientational disorder about 13 deg within the nanocrystals.

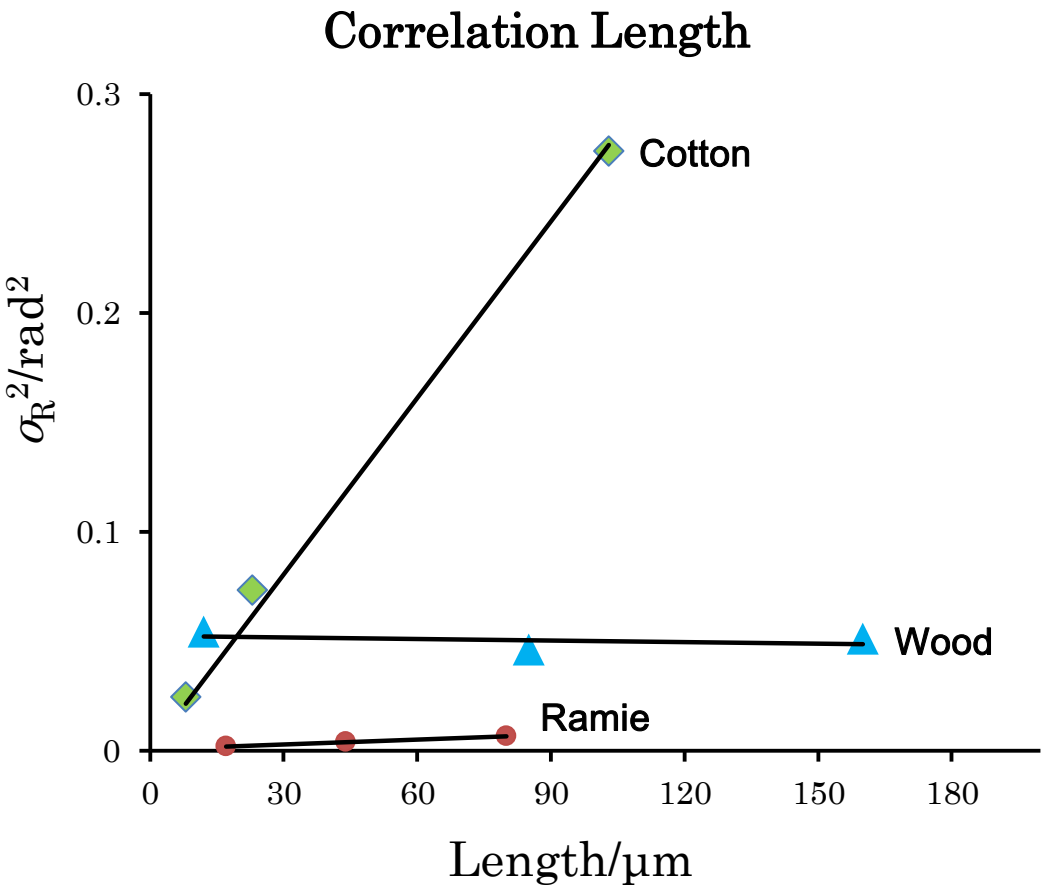

Fig. 14 Plot of the standard deviations σ_R^2 determined from Fig. 4(b), Fig. 10(b), Fig. 13(b) of the rotating samples as a function of the size *L* of the CWs.

4.4 Conclusion

CWs prepared from cotton cellulose (Whatman CF11) were aligned under static or rotating magnetic fields and the distribution of CNCs in the CW was analyzed using X-ray diffraction. By the analyses of the diffraction patterns of magnetically oriented samples, one prepared under static and the other prepared under rotating magnetic fields, it was found that the *c*-axes of the CNCs were distributed uniaxially in the CW. It was also found that the orientational degree of CNCs in the CW increased with decreasing CW size. The anisotropic magnetic susceptibility $\langle \chi_a \rangle$ of the CWs was expressed by an exponential function of the size σ_R^2 of the CWs, from which the correlation length was determined to be ca. σ_R^2 = 142 μm. The method presented in this chapter is also useful for the analysis of orientational orders in other fibrous materials including biomacromolecules as well as synthetic polymers that exhibit hierarchical suprastructures. The method allows us to investigate the orientational order in a macrofiber at arbitrary scales by magnetically aligning the small fragments segmented from the macrofiber. The method has been applied to ramie and wood cellulose to study the orientational distribution of nanocrystals in CW, to determine the correlation length.

APPENDIX

A. Derivation of Eq. (1). Let us consider the distribution of the reciprocal vector $\mathbf{G}$ for (200) on the surface of the reciprocal lattice sphere formed by $\mathbf{G}$, as shown in **Fig. 6(b)**. The experimentally observed azimuthal profile of this distribution is related to the line density f of the vector $\mathbf{G}$ on the intersection circle formed by the Ewald sphere and this reciprocal lattice sphere. The reciprocal lattice sphere and the intersection circle are drawn schematically in **Fig. A** with respect to the *xyz*-coordinates, where the X-ray beam impinged along the *y*-direction. The orientation of the χ_1-axis (parallel to the applied magnetic field) of the sample is denoted by a unit vector **n** expressed by polar coordinates (γ, δ). If **n** is set parallel to the *z*-axis, then $\gamma = 0$. Let us consider a point P on the intersection circle, defined by the azimuthal angle β. At P, the density $f(\beta)$ is proportional to $1/\sin\phi$, with ϕ being the angle between **n** and the line $\overrightarrow{\mathrm{OP}}$. By a simple calculation, we obtain $\cos\phi$ as a function of β as follows:

$$\cos\phi = (R/G)(\cos\beta\cos\gamma + \sin\beta\sin\gamma\cos\delta) + (1-(R/G)^2)^{1/2}\sin\gamma\sin\delta\,, \qquad \text{(A1)}$$

where G is the radius of the reciprocal lattice sphere and $R = (2\pi/\lambda)\sin 2\theta$, with λ being the wavelength of the X-ray and 2θ, the diffraction angle of (200). In **Fig. 6(b)**, fluctuations of the *c** axes are not considered. However, such a fluctuation exists, as reflected in the broadening observed for the samples prepared by sample rotation [**Fig. 4(b)**]. Therefore, the function $f(\beta)$ should be convoluted with a Gaussian function $h(\beta) = (2\pi\sigma^2)^{-1/2}\exp(-\beta^2/2\sigma^2)$ representing these fluctuations, where the standard

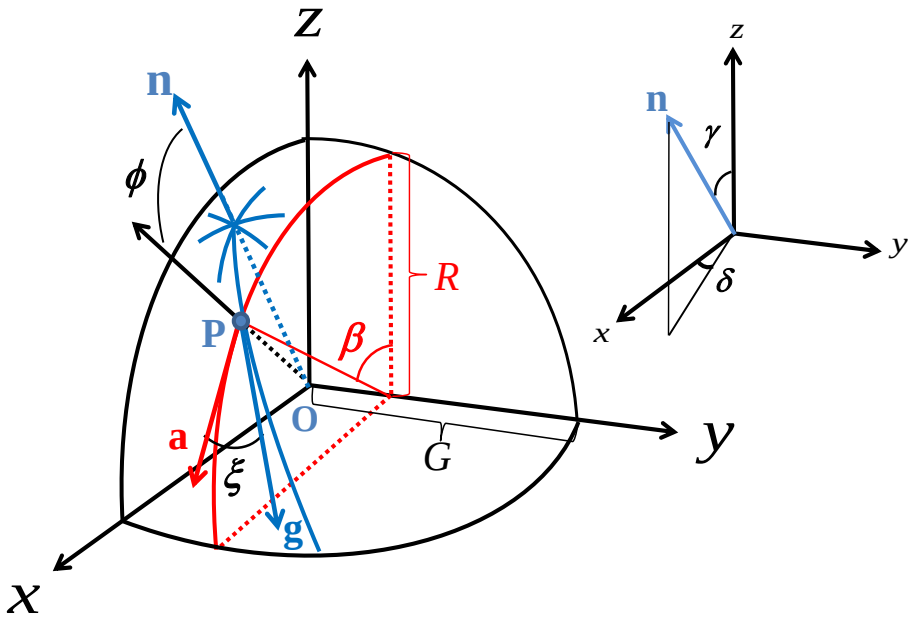

Fig. A Definitions of the angles γ, δ, β, ϕ, and ξ. The angles γ and δ (shown at the top right) describe the direction of the unit vector **n** with respect to the *xyz*-coordinates. The direction of **n** corresponds to the direction of the magnetic field **B** in Fig. 6. The point P is located on the intersection circle formed by the reciprocal lattice sphere of radius *G* and the Ewald sphere. The location of P projected on the azimuthal scan is denoted by the angle β. The line $\overrightarrow{\mathrm{OP}}$ makes an angle ϕ with respect to the vector **n**. The tangential vectors **a** and **g**

deviation σ depends on the angle ξ shown in **Fig. A**. The angle ξ is defined as the angle between the tangential vectors $\mathbf{a}$ and $\mathbf{g}$ at P with respect to the intersection circle and the great circle formed by $\mathbf{G}$, respectively. We obtain

$$\sigma(\beta) = \sigma_{\mathrm{R}} / \sin\xi(\beta), \qquad \text{(A2)}$$

where σ_{R} is the standard deviation determined from the Gaussian distribution of the samples prepared by sample rotation, as shown in **Fig. 4(b)**, and the angle $\xi(\beta)$ is expressed as a function of β:

$$\begin{aligned}\cos^{-2}\xi(\beta) = \{&1-\sin^2\gamma\sin^2\delta - 2(R/G)(1-(R/G)^2)^{1/2}\sin\gamma\sin\delta(\cos\beta\cos\gamma+\cos\delta\sin\beta\sin\gamma)\\ &+(R/G)^2(-\cos^2\beta\cos^2\gamma - 2\cos\beta\cos\gamma\cos\delta\sin\beta\sin\gamma+\sin^2\gamma(-\cos^2\delta\sin^2\beta+\sin^2\delta))\}\\ &(\cos\gamma\sin\beta-\cos\beta\cos\delta\sin\gamma)^{-2}.\end{aligned}$$

(A3)

Using Eq. A3, $\sigma(\beta)$ in Eq. A2 is determined. Now, the Gaussian function to be used for the convolution is expressed by

$$h(\beta-\beta_0) = \frac{1}{\sqrt{2\pi\sigma^2(\beta_0)}}\exp\left(-\frac{(\beta-\beta_0)^2}{2\sigma^2(\beta_0)}\right). \qquad \text{(A4)}$$

The calculated azimuthal profile to be compared with the experimentally observed profile is given by the following convolution:

$$F(\beta) = \int_{-\infty}^{\infty} f(\beta_0)\, h(\beta - \beta_0) d\beta_0 \,. \qquad \text{(A5)}$$

If $\gamma = 0$, $f(\beta)$ and $\cos^{-2}\xi(\beta)$ are reduced to

$$f(\beta) \propto \frac{1}{\sin\phi} = \frac{1}{\sqrt{1-\cos^2\phi}} = \frac{1}{\sqrt{1-(R/G)^2\cos^2\beta}}\,, \qquad \text{(A6)}$$

and

$$\cos^{-2}\xi(\beta) = \{1-(R/G)^2\cos^2\beta\}\sin^{-2}\beta\,, \qquad \text{(A7)}$$

respectively.

B. Derivation of Eq. (3). Let us suppose that the *c*-axes of the CNCs are uniaxially distributed in a CNF (or its aggregate) and its magnetic susceptibilities are $\chi_{||}$ and $\chi_{\perp}$ in the directions parallel and perpendicular to the CNF axis, respectively. The susceptibility tensor $\boldsymbol{\chi}_{\mathrm{P}}$ with respect to the particle coordinates is expressed by

$$\boldsymbol{\chi}_{\mathrm{P}} = \begin{pmatrix} \chi_{\perp} & 0 & 0 \\ 0 & \chi_{\perp} & 0 \\ 0 & 0 & \chi_{||} \end{pmatrix}. \qquad \text{(B1)}$$

This tensor is transformed to $\boldsymbol{\chi} = {}^{\mathrm{t}}\mathbf{A}\boldsymbol{\chi}_{\mathrm{P}}\mathbf{A}$ with respect to the laboratory *xyz*-coordinates by using a transformation matrix $\mathbf{A}$ expressed by the Euler angles ϕ, θ, ψ, where the $Z_1X_2Z_3$-convention is used (see H. Goldstein, Classical Mechanics Third edition,

(Pearson Education, Inc. 2002) Chap. 4). Here, θ is the angle of the CNF axis with respect to the axis of the whisker (CW) that directs the *z*-axis. We assume that the distribution of θ of the CNFs in a CW is expressed by a Gaussian distribution with the standard deviation σ_{R} (rad) as follows:

$$P(\phi,\theta,\psi)\sin\theta\,d\phi\,d\theta\,d\psi = K\left(\exp(-\theta^2/2\sigma_{\mathrm{R}}^2)+\exp(-(\theta-\pi)^2/2\sigma_{\mathrm{R}}^2)\right)\sin\theta\,d\phi\,d\theta\,d\psi \qquad \text{(B2)}$$

with

$$K^{-1} = \int_0^{2\pi} d\phi \int_0^{2\pi} d\psi \int_0^{\pi} \left(\exp(-\theta^2/2\sigma_{\mathrm{R}}^2)+\exp(-(\theta-\pi)^2/2\sigma_{\mathrm{R}}^2)\right)\sin\theta\,d\theta \qquad \text{(B3)}$$

If σ_{R} is not very large, the above distribution is a good approximation. Now, each component of χ is averaged using this distribution function. The average is calculated by

$$\left\langle \chi_{\mathrm{ij}} \right\rangle = \iiint \chi_{\mathrm{ij}} P(\phi,\theta,\psi)\,\sin\theta\,d\phi\,d\theta\,d\psi \qquad \text{(B4)}$$

with χ_{ij} being the ij-component of the tensor χ. The averages of the off-diagonal components vanish and $\langle \chi_{11} \rangle = \langle \chi_{22} \rangle$. The average anisotropic susceptibility (parallel minus perpendicular) is defined by $\langle \chi_{\mathrm{a}} \rangle \equiv \langle \chi_{33} \rangle - \langle \chi_{11} \rangle$. The resulting $\langle \chi_{\mathrm{a}} \rangle$ is expressed by

$$\langle \chi_a \rangle = (\chi_{||} - \chi_{\perp}) \exp\left(-2.6\sigma_R^2\right), \qquad \text{(B5)}$$

in good approximation up to $\sigma_R \cong 1.4$.

References

[1] Azizi Samir, M. A. S.; Alloin, F.; Dufresne, A. *Biomacromolecules*, **2005**, *6*, 612–626.

[2] Klemm, D.; Heublein, B.; Fink, H.-P.; Bohn, A. *Angew. Chem. Int. Ed*. **2005**, *44*, 3358–3393.

[3] Habibi, Y.; Lucia, L. A.; Rojas, O. J. *Chem. Rev*. **2010**, *110*, 3479–3500.

[4] Moon, R. J.; Martini, A.; Nairn, J.; Simonsen, J.; Youngblood, J. *Chem. Soc. Rev.*, **2011**, *40*, 3941–3994.

[5] Beck-Candanedo, S.; Roman, M.; Gray, D. G. *Biomacromolecules*, **2005**, *6*, 1048–1054.

[6] Elazzouzi-Hafraoui, S.; Nishiyama, Y.; Putaux, J.-L.; Heux, L.; Dubreuil, F.; Rochas, C. *Biomacromolecules*, **2008**, *9*, 57–65.

[7] Rowland, S. P.; Roberts, E. J. *J. Polym. Sci. Part A: Polym. Chem*. **1972**, *10*, 2447–2461.

[8] Anderson, D. B.; Kerr, T. *Ind. Eng. Chem.* **1938**, *30*, 48–54.

[9] Cave, I. D. *Wood Sci. Tech*. **1997**, *31*, 225–234.

[10] Sugiyama, J.; Chanzy, H.; Maret, G. *Macromolecules* **1992**, *25*, 4232–4234.

[11] Revol, J. F.; Godbout, L.; Dong, X. M.; Gray, D. G.; Chanzy, H.; Maret, G. *Liq. Cryst*. **1994**, *16*, 127–134.

[12] Dong, X.-M.; Gray, D. G. *Langmuir* **1997**, *13*, 3029–3034.

[13] Cranston, E. D.; Gray, D. G. *Sci. Technol. Adv. Mater*. **2006**, *7*, 319–321.

[14] Kvien, I.; Oksman, K. *Appl. Phys*. *A*. **2007**, *87*, 641–643.

[15] Kimura, F.; Kimura, T.; Tamura, M.; Hirai, A.; Ikuno, M; Horii, F. *Langmuir* **2005**, *21*, 2034–2037.

[16] Kimura, F.; Kimura, T. *Sci. Technol. Adv. Mater.* **2008**, *9*, 024212.

[17] Kimura, F.; Kimura, T. *J. Phys: Conf. Ser*. **2009**, *156*, 012002.

[18] Pullawan, T.; Wilkinson, A. N.; Eichhorn, S. J. *Biomacromolecules*, **2012**, *13*, 2528–2536.

[19] Bordel, D.; Putaux, J.-L.; Heux, L. *Langmuir* **2006**, *22*, 4899–4901.

[20] Habibi, Y.; Heim, T.; Douillard, R. *J. Polym. Sci. Part B: Polym. Phys*. **2008**, *46*, 1430–1436.

[21] Nishiyama, Y.; Kuga, S.; Wada, M.; Okano, T. *Macromolecules* **1997**, *30*, 6395–6397.

[22] Kimura, T. *Polm. J.* **2003**, *35*, 823–843.

[23] Nye, J. F. Physical Properties of Crystals; Clarendon Press: Oxford, 1985; ch. 3.

[24] Kimura, T.; Yoshino, M.; Yamane, T.; Yamato, M; Tobita, M. *Langmuir* **2004**, *20*, 5669–5672.

[25] Akiyama J.; Hashimoto, M.; Takadama, H.; Nagata, F. Yokogawa, Y.; Sassa, K.; Iwai, K.; Asai, S. *Materials Trans*. **2005**, *46*, 203–206.

[26] Akiyama, J.; Asano, H.; Iwai, K.; Asai, S. *Materials Trans*. **2008**, *49*, 787–791.

[27] Nishiyama, Y.; Sugiyama J.; Chanzy, H.; Langan, P. *J. Am. Chem. Soc*. **2003**, *125*, 14300–14306.

[28] Nishiyama, Y.; Langan, P.; Chanzy, H. *J. Am. Chem. Soc*. **2002**, *124*, 9074–9082.

[29] Gupta, R. R. “Landolt-Bornstein”; Hellwege, H.-H., Hellwege, A. W., Eds.; Springer Verlag: Berlin, 1986; vol. II/16, ch. 8.

[30] Nishiyama, Y. *J. Wood Sci*. **2009**, *55*,241–249.

[31] Nishiyama, Y.; Kim, U.-J.; Kim, D.-Y.; Katsumata, K. S.; May, R. P.; Langan P. *Biomacromolecules* **2003**, *4*, 1013–1017.

[32] Rollins, M. L.; Tripp, V. W. *Text. Res. J*. **1954**, *24*, 345–357.

Chapter 5

Summary

In Chapter 2, *in-situ* or *ex-situ* X-ray diffraction study on 1-dimensionally oriented microcrystals for determining magnetic anisotropy of cellobiose is described. In order to achieve high degree of magnetic orientations, we need to know magnetic anisotropy. However, the anisotropy of many materials is not known; thus, a facile method to determine the anisotropy of materials had long been strongly desired. The magnetic anisotropy results in the anisotropic orientation fluctuation of microcrystals under magnetic field. The fluctuation can be reflected on diffraction spot broadening. Therefore, a method that allows determination of magnetic anisotropy by in-situ or ex-situ X-ray diffraction was developed. The method was applied to determine the magnetic anisotropy of cellobiose.

In Chapter 3, single-crystal NMR spectroscopic study on 3-dimensionally oriented microcrystals for determining chemical shift tensors of C1 and C1' carbons of cellobiose is described. Single-crystal NMR technique is a powerful method that allows determination of the chemical shift tensor, which is a useful parameter for NMR crystallography and local structure analyses. However, this technique requires large single crystals (mm scales). The bottleneck of this technique has now been overcome by using 3-dimensionally magnetically aligned microcrystals whose sizes can be as small as several hundred nanometers in my experimental setup. In particular, a facile method is developed to determine chemical shift tensors by using the aligned microcrystals, combined with 2D solid-state NMR technique.

In Chapter 4, *ex-situ* X-ray diffraction study on 1-dimensionally oriented cellulose whiskers is perfomred for the analyses of hierarchical suprastructures. Nanocrystal distribution in cellulose whiskers from different species are elucidated by applying X-ray diffraction on oriented whiskers. This novel idea can also be used in other polymers.

Publication List

Chapter 2

G. Song, K. Matsumoto, K. Fujita, F. Kimura, and T. Kimura.

"Determination of Ratio of Diamagnetic Anisotropy of a Biaxial Crystal by X-ray Diffraction Measurement".

Jpn. J. Appl. Phys., **51**, 060203-1-3, 2012.

Chapter 3

G. Song, R. Kusumi, F. Kimura, T. Kimura, K. Deguchi, S. Ohki, T. Fujito, and T. Shimizu.

"Single-crystal NMR Study of 13C Chemical Shift Tensor of Cellobiose via Magnetically Oriented Microcrystal Array".

Submitted.

Chapter 4

G. Song, F. Kimura, T. Kimura, and G. Piao.

"Orientational Distribution of Cellulose Nanocrystals in a Cellulose Whisker As Studied by Diamagnetic Anisotropy".

Macromolecules, **46**, 8957-8963, 2013.

Other contributions

T. Kimura, **G. Song**, K. Matsumoto, K. Fujita, and F. Kimura. "Determination of Anisotropic Diamagnetic Susceptibility Using X-ray Diffraction". *Jpn. J. Appl. Phys*., **51**, 040202-1-3, 2012.

R. Kusumi, F. Kimura, **G. Song**, T. Kimura. “Chemical Shift Tensor Determination using Magnetically Oriented Microcrystal Array (MOMA): ^{13}C Solid-state CP NMR without MAS”. *J. Magn. Reson*., **223**, 68–72, 2012.

T. Kimura, T. Tanaka, **G. Song**, K. Matsumoto, K. Fujita, and F. Kimura. “Orientation Fluctuation of Microcrystals under Three-Dimensionally Constraining Dynamic Magnetic Field”. *Cryst. Growth Des*., **13**, 1815−1819, 2013.

K. Matsumoto, F. Kimura, **G. Song**, S. Yamane, H. Kikuchi, T. Tanaka, S.Higuchi, N. Kitamura, and T. Kimura. “Crystal System Determination from X-ray Diffraction of Magnetically Oriented Microcrystal Suspension”. *Cryst. Growth Des*., Published online, 2014.

Acknowledgements

The sincerest thanks surely go to Prof. T. Kimura at Laboratory of Fibrous Biomaterials, Kyoto University. All the research is under his patient and kind guidance.

The author would like to thank Dr. F. Kimura at Laboratory of Fibrous Biomaterials, Kyoto University. The progress always goes with her kind help and encouragements. The sincere thanks are given to her.

The author expresses his thanks to Professor Y. Nishio at Laboratory of Chemistry of Composite Materials, Kyoto University, and Professor T. Takano at Laboratory of the Chemistry of Biomaterials, Kyoto University for their critical reading of this thesis manuscript and significant suggestions.

The thanks are given to Assistant Professor R. Kusumi for his kind help during the study. The thanks also go to Associate Professor M. Wada for his kind help during the research.

The author wishes to express his gratitude to Professor G. Piao at School of Polymer Science and Engineering, Qingdao University of Science and Technology for his continuous support and encouragement.

The author would like to thank the members at Laboratory of Fibrous Biomaterials for their kind help and co-operation.

The author acknowledges the members in high-field NMR group, National Institute for Materials Science for their kind corporation of the NMR work.

Finally, the author would like to thank his family and friends for their continuous support and encouragement.